INVESTIGATION OF MULTIFUNCTIONAL, ADDITIVELY MANUFACTURED STRUCTURES USING FUSED FILAMENT FABRICATION

A Dissertation

Submitted to the Faculty

of

Purdue University

by

Trevor J. Fleck

In Partial Fulfillment of the

Requirements for the Degree

of

Doctor of Philosophy

May 2020

Purdue University

West Lafayette, Indiana

THE PURDUE UNIVERSITY GRADUATE SCHOOL
STATEMENT OF DISSERTATION APPROVAL

Dr. Jeffrey Rhoads, Chair

School of Mechanical Engineering

Dr. George Chiu

School of Mechanical Engineering

Dr. Marcial Gonzalez

School of Mechanical Engineering

Dr. Weinong Chen

School of Aeronautics and Astronautics and School of Materials Engineering

Approved by:

Dr. Nicole Key

Head of the School Graduate Program

ACKNOWLEDGMENTS

I would like to thank my advisor and mentor, Dr. Jeffrey Rhoads for guiding me through both my undergraduate and graduate studies while at Purdue University.

I would also like to thank my friends and family for their constant support that has allowed me to get to this point in my graduate studies. In particular, I would like to thank my wife, Valarie, for always being there for me and supporting me selflessly over the past 3 years.

I would also like to thank Purdue University for funding this work.

TABLE OF CONTENTS

LIST OF TABLES

LIST OF FIGURES

Figure Page

Figure Page

ABSTRACT

Fleck, Trevor J. Ph.D., Purdue University, May 2020. Investigation of Multifunctional, Additively Manufactured Structures using Fused Filament Fabrication. Major Professor: Jeffrey F. Rhoads, School of Mechanical Engineering.

From its advent in the 1980s until the 2000s, many of the advances in additive manufacturing (AM) technology were primarily focused on the development of various 3D printing techniques. During the 2000s, AM came to a juncture where these processes were well developed and could be used effectively for rapid prototyping purposes; however, the ability to produce functional components that could reliably perform in a given system had not been fully achieved. The primary focus of AM research since this juncture has been to transition AM from a rapid prototyping technique to a legitimate means of mass manufacturing end-use products. In order to make this happen, two significant areas of research needed to be advanced. The first area focused on advancing the limited selection and functionality of the materials being used for AM. The second area focused on the characterization of the end-use products comprised of these new materials.

The primary goals of the work described in this document are to substantially further the field of the additive manufacturing by developing new functional materials and subsequently characterizing the resultant printed components. The primary focus of the first two chapters (Chapters 2 and 3) is to further characterize an energetic material system comprising of aluminum (Al) particles embedded in a polyvinylidene fluoride (PVDF) binder, which has been shown to be compatible with AM. This material system has the ability to be implemented as a lightweight multifunctional energetic structural material (MESM); however, significant characterization of its structural energetic properties is needed to ensure reliable MESM performance. First, variations of a previously demonstrated Al/PVDF filament were investigated in order to determine the effect of material constituents on the structural energetic properties of the material. Seven different Al/PVDF formulations, with various particle loadings and particle sizes, were considered. The modulus of elasticity and ultimate strength for

the seven formulations were obtained via quasi-static tensile testing of 3D printed dogbones. The energetic performance was quantified via burning rate measurements and differential scanning calorimetry (DSC) of 3D printed samples. Next, variations in the AM process were made and the effect of print direction on the same properties was determined. Once viable MESM performance was quantified, representative structural elements were printed in order to demonstrate the ability to create structural energetic elements. During quasi-static tensile testing, it was observed that aligning the load direction perpendicular to the print direction of the component resulted in inferior mechanical properties. This reduction in mechanical properties can be attributed to the lack of continuity at material interfaces, a well studied phenomena in AM.

This phenomena is the primary focus of the next two chapters (Chapters 4 and 5), which investigate the polymer healing process as it pertains to fusion-based material extrusion additive manufacturing, also known as fused filament fabrication (FFF). In the context of the FFF process, the extent of the polymer healing, or lack thereof, at the layer interface is known to be thermally driven. Chapter 4 quantifies the relationship between the reduction in mechanical properties and the temperature of the previously deposited layer at the time the subsequent layer is deposited. This relationship gives insight into which parameters should be closely monitored during the FFF process. The following chapter investigates incorporating plasma surface treatment as a means to improve the reduced mechanical properties seen in Chapter 3 and 4. As plasma surface modification can affect various stages of the polymer healing process, a variety of experiments were completed to determine which mechanisms of the plasma treatment were significantly affecting the mechanical properties of the FFF components. The thermal history was analyzed and it was hypothesized that enhanced diffusion at the layer interface was not a significant contributor to, but a rather a detractor from, the improved mechanical properties in this system. A variety of tests investigating how the plasma treatment was affecting the wettability of the surface were performed and all of the tests indicated that the wettability was increased during treatment and was likely the driving mechanism causing the improvement seen in the mechanical properties. These tests give some initial insight into how to successfully pair plasma treatment capabilities

with FFF systems and give insights into how that plasma treatment can affect the polymer healing process in FFF applications.

1. INTRODUCTION

1.1 Background

1.1.1 A Brief Review of Additive Manufacturing

From its advent in the 1980s until the 2000s, many of the advances in additive manufacturing (AM) technology were primarily focused on the development of various 3D printing techniques, all of which manufacture components one layer at a time [1–3]. This method of manufacturing allows for geometric flexibility that is not offered by traditional manufacturing. Over this time period, AM techniques matured from experimental manufacturing processes to well-developed processes, which are common in industry as a means of rapid prototyping. Of the main AM techniques, stereolithography (SLA) was the first process to be patented in 1984, utilizing UV light to selectively solidify a photocuring polymer layer-by-layer [1]. Selective laser sintering (SLS) was the first AM process to produce 3D metal components, creating complex geometrical structures by sintering feedstock particles to previously deposited material [1]. The final notable 3D printing method developed in this time frame was fused filament fabrication (FFF), which eventually became the most common AM method due to its relatively faster print times and lower cost of equipment. These advantages of FFF can be attributed to the simplicity of the method of deposition, wherein a heated nozzle is used to melt and deposit a polymer feedstock in order to fuse it to a previous layer [1–3].

During the 2000s, AM came to a juncture where these processes were well developed and could be used effectively for rapid prototyping purposes. However, the ability to produce components that could reliably perform a function in a given system, referred to as "functional" components in this document, had not been fully achieved. The primary focus of AM research since this juncture has been to take AM from a rapid prototyping technique to a legitimate means of mass manufacturing end-use products. In order to make this happen, two areas of research needed to be advanced. The first area focused on advancing the limited

functionality of the materials being used for AM. While AM had become efficient at producing 3D components out of standard materials, such as acrylonitrile butadiene styrene (ABS) or polylactic acid (PLA), in practice, these materials have limited functionality beyond the purposes of rapid prototyping. Recent advances in this area include functional feedstocks coming on the market, such as polycarbonate thermoplastics with higher strength and toughness [4], conductive polymers for 3D printed electronics [5], and chemically resistant polymers compatible with chemically hazardous environments [6]. While there have been many significant advances in feedstock development for additive manufacturing, there are still many classes of materials that can be developed to be compatible with the FFF process.

In addition to enhancing the functionality of the feedstock materials, the second significant area of AM research focused on the characterization of the end-use products comprised of these materials. In order for AM components to be implemented within systems, the performance of parts must be well characterized. Additionally, how the various parameters of the AM process affect this performance must be well understood. The process of proving that additively manufactured components will perform as desired is typically done through post-print characterization. As previously mentioned, one of the main advantages of AM is the fact that it can be used to create complex geometrical structures by constructing them layer-by-layer [1]. Consequentially, the resultant interfaces of these layers cause issues with reduced part functionality. For example, with structural elements, the lack of continuity at the material interface results in stress concentrations or other defects which in turn result in inferior strength in the build direction. This tends to make the material's mechanical properties exhibit heavily anisotropic behavior, making their structural performance more challenging to predict [7–10]. Another example would be with conductive 3D printed components. The same lack of continuity at the layer interfaces results in inferior conductivity in certain directions [11]. Many efforts in AM research focus on how to overcome the inferior performance of AM components and make them comparable to, and therefore viable replacements for, traditionally manufactured parts. While there have been many advances in these two areas (i.e. in the development of new materials and the characterization/improvement of those materials) over the past decade, one class of materials that has received little attention until recently is energetic materials. The work presented in this document advances

additive manufacturing by contributing to both of the highlighted areas by introducing new functional materials and characterizing, and improving, the mechanical properties of the resultant printed components, all within the context of the additive manufacturing of energetic materials.

1.1.2 Additive Manufacturing of Energetic Materials

Energetic materials are a type of functional material that will either deflagrate or detonate when provided an ignition source. All energetic materials contain both a fuel and an oxidizer in the same material. The close proximity of the fuel to the oxidizer allows them to chemically react with one another, yielding byproducts that can be put to functional use. Energetic materials can be classified as either propellants, pyrotechnics, or explosives, depending on their function [12, 13]. Applications of propellants range from space applications [14] to microthrusters [15] and air bag initiators [16]. Pyrotechnics have been used in fireworks, smoke producers, flares, and other military applications [13, 17]. The functionality of an energetic material component has been shown to be heavily dependent on geometry [18]. The ability to control the performance of energetic materials based on geometric manipulation has made additive manufacturing very attractive for this class of materials [13, 18]. In addition to the benefits of reduced waste and safer handling, additive manufacturing processes could be used to tune the performance of these materials and tailor them for a specific function.

Due to this list of potential benefits of pairing additive manufacturing with energetic materials, several efforts have been made in the last 5-10 years to print energetic material. The higher processing temperatures, paired with the inability to handle high solids loadings, of the predominant AM techniques previously discussed have deterred efforts of pairing this class of materials with SLS, FFF, or SLA methods. Figure 1.1 depicts the most common AM techniques that have been shown to pair well with energetic materials. The first row identifies the method, with the second and third rows identifying the major benefits and the significant drawbacks of the method. The first two methods shown in Figure 1.1 have been demonstrated by Murray et al. [19] and Huang et al. [20] to be capable of depositing functional amounts of energetic material. However, while these methods are effective (particularly inkjet printing)

in terms of material selection, they are primarily used to create 2D geometries. The next and most popular method for additively manufacturing energetic materials to date has been direct-write methods [18,21,22], where solvent is added to materials in order to create a thick paste. This thick paste is then extruded out of a nozzle, typically utilizing back pressure or a piston. After the solvent dries, the deposited solids left behind form the 3D printed structure [23]. While direct-write methods are compatible with a wider variety of energetic materials, issues arise when trying to print more than a few layers of material. Essentially, the print speed needs to be slow enough to allow for the solvent to completely evaporate before the subsequent layer is deposited. This results in either extremely long print times, or post-print "sagging", where extra solvent is left from printing process and leaves a deformed final product after evaporation. Despite the challenges present with this printing technique, many significant advances in the additive manufacturing of energetic materials have been made using direct write. Research by Durban et al. demonstrated the ability to create complex 3D structures out of thermite materials, a well characterized type of energetic material that can be used in a variety of applications [22]. This method has also been shown to be viable for depositing fluoropolymer inks by Ruz-Nuglo, Groven, and Mezger, who studied how the process parameters of direct-write systems affect combustion performance [18, 21]. The fourth box shows vibration-assisted printing (VAP), which is a modified version of direct write in which ultrasonic vibrations are applied to the nozzle in order to induce the flow of a highly viscous material. The ability to induce flow with the ultrasonic vibrations reduces the amount of solvent needed for extrusion, eliminating many of the concerns previously discussed. Gunduz et al. [24] and McClain et al. [25] have demonstrated the abilities of this method to print energetic materials. While there is no significant complication with this method, VAP is still in its infancy and significant characterization of the printing process is still needed.

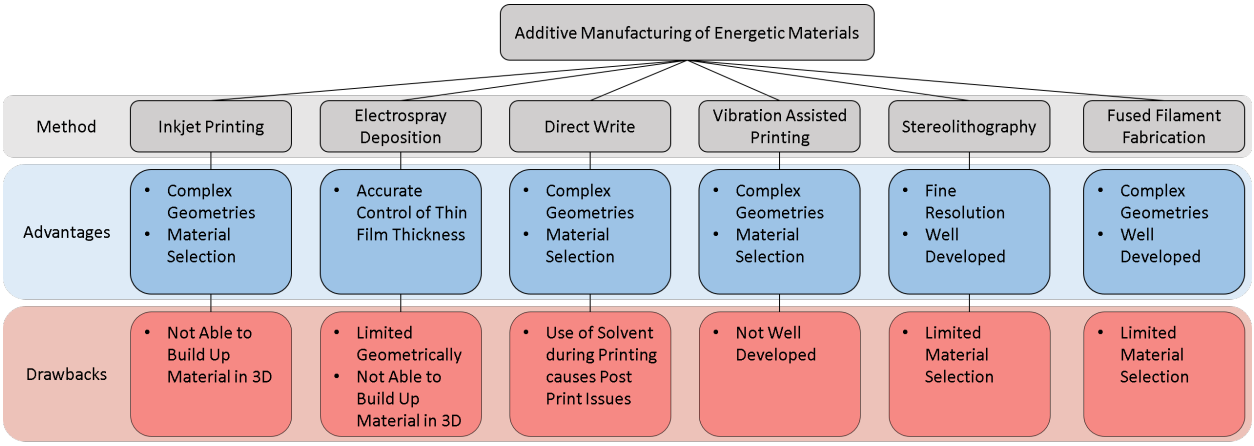

Figure 1.1. This chart highlights all of the methods that have been reported in open literature for the additive manufacturing of energetic materials.

More recently, efforts have been made to adapt the predominant AM techniques, such as SLA and FFF, to be compatible with energetic materials [13, 26, 27]. Straathof et al. have successfully paired energetic materials with the SLA process by developing propellant compositions that are compatible with the photopolymerization process [26]. In the context of FFF, while limited to only a few certain types of energetic materials, there are still certain energetic materials whose application space could be broadened by pairing it with additive manufacturing. The material system showing the most promise to this point with FFF methods is metal-fluoropolymer energetic materials [13, 27]. A prelude to this work by Fleck et al. demonstrated the ability to 3D print a reactive material using a commercially available 3D printer with printability comparable to common 3D printing materials [13]. Bencomo et al. also showed success using this method, 3D printing a variety of Al/PVDF formulations and determining the effect of the formulation constituents on the electroactivity and the rheology of the material [27].

1.1.3 Characterization and Improvement of the Mechanical Properties of Additively Manufactured Components

While the aforementioned efforts in the field of the additive manufacturing of energetic materials have done a lot in terms of developing new types of functional materials (the first main area of AM research previously highlighted), much work still needs to be done in terms of post-print energetic component characterization. In the case of the Al/PVDF material developed for FFF by Fleck et al. [13], the ability to print the material was successfully demonstrated, but significant work is still needed before 3D printed Al/PVDF components can be integrated in with a system. One of the main application spaces for this material is to use it as a multifunctional energetic structural material (MESM). These materials have dual functionality, providing both structural and energetic capabilities for a system [28–30]. However, in order for 3D printed Al/PVDF structures to be used reliably, both of these functionalities must be well characterized. Additionally, there needs to be a thorough understanding of which FFF process and material parameters affect those functionalities.

While the literature on post-print characterization of 3D printed energetic materials is limited, the extensive prior art on how the AM process effects the mechanical properties of standard, inert materials provides a logical path forward for this work [31]. It is now common for custom supports, fixtures, and components to be 3D printed and utilized as structural elements. There has been extensive research showing that many parameters in the AM process can have a significant effect on mechanical properties, such as the modulus of elasticity and ultimate strength [31–33] . It has been shown that the strength of the material is dependent on the print direction, inherently making AM components strongly anisotropic. Other parameters such as print speed [31], infill percentage [33], and layer height [31] have also been shown to effect the mechanical properties of these materials in some capacity. In many cases, the extent to which the AM process effects the structural properties is dependent on the material system. This indicates that whenever a new functional material is developed by additive manufacturing, a set of standard tests need to be conducted in order to determine the extent to which the AM process effects the functionality of the material. In addition to understanding the material-process-function relationships of these additively manufactured

energetic materials, work also needs to be done to improve the inferior properties of these additively manufactured components. The limited work in the characterization of additively manufactured energetic materials has shown that the resultant mechanical properties are insufficient for their intended use. The work in this document focuses on how the FFF process affects the structural energetic capabilities of the Al/PVDF material, and in particular, explores which parameters need to be carefully controlled to ensure reliable MESM performance. Additionally, the mechanism that causes the reduced mechanical properties is investigated, and efforts are made to improve the mechanical properties of additively manufactured components.

1.2 Project Goals

Chapter 2 of this document seeks to characterize the Al/PVDF formulations that are compatible with the FFF 3D printing method and gain an understanding of how the material performs as an MESM. Seven different formulations were chosen for this study, with varying solids loadings and particle sizes. This chapter gives insights into the Al/PVDF material's ability to act as an MESM before varying the AM process. Additionally, material selection plots were developed, allowing for visualization of MESM performance during the design phase.

Once the dependence of structural energetic properties on the material formulation was understood, variations in the AM process were made to gain an understanding of how the AM process can be used to selectively tailor the structural energetic performance of these materials. The purpose of the next chapter of this document was to develop a test plan that should be used for all AM structural energetics in order to understand the extent of this dependence. As the FFF process has many parameters, all of which can affect the structural capabilities, the scope of experimentation was limited to the parameters shown in literature to have the largest effect on mechanical properties. The same testing procedure as in Chapter 2 was used, in which samples were printed in two different, perpendicular directions (0° and 90° raster orientations). Beyond the dependence on print direction, two different truss designs were printed out of the Al/PVDF material in order to simulate realistic

structural energetic elements. The two different trusses were tested using a 3-point bending apparatus and demonstrated the ability to control the structural properties of these realistic elements during the print process.

The results obtained from the print direction study showed a dependence of the material's mechanical properties on the print direction when transitioning from a 0° to a 90° raster orientation. This was determined to be the result of a lack of continuity at the layer-to-layer interface, which in turns results in a reduction of strength. This effect is something that has been noted extensively in literature, but has not been fully studied to this point. The final two chapters of this document investigate the layer-to-layer interfaces in 3D printed components. Chapter 4 focuses on a set of experiments that seeks to quantify the reduction of strength at the layer interface and gain a better understanding of the underlying mechanism causing this reduction. In order to quantify the extent to which the layer-to-layer adhesion is thermally driven [36, 37], two types of samples were printed with various wait times in order to allow a controlled amount of cooling to take place. These samples were then mechanically tested in order to correlate the amount of cooling to the overall strength of the structure. These tests give insight into which impactful print parameters to be aware of during the AM process such as print speeds, feature sizes, and print direction, as they will all impact the amount of interlayer cooling to some extent.

Chapter 5 investigates the use of plasma surface treatment as a means to overcome the reduced mechanical performance of FFF structures, as seen in Chapters 3 and 4. Plasma treatment has been widely used in industry as a means of surface modification for the purposes of increasing surface adhesion properties. The goal of this work was to incorporate plasma surface treatment onboard a traditional FFF printer in order to improve the mechanical properties during the printing process. Further work sought to isolate the underlying mechanism that was increasing these properties in order to better understand how to apply plasma surface modification to other FFF material systems. This included investigating the diffusion kinetics at the interface, as well as the wettability of the polymer surface, in order to better understand how the plasma modification was affecting these aspects of the polymer healing process.

As a whole, this work advances the field of additive manufacturing by contributing to both the development of novel AM materials, as well as the development of material-process-function relationships that help predict AM component performance. Additionally, these efforts seek to enhance the functionality of AM components in order to increase their likelihood of being used as end-use products. While most of this work was done in the context of the additive manufacturing of energetic materials, the impact of this work is relevant to many other material systems and application areas as well.

2. INFLUENCE OF AL/PVDF CONSTITUENTS ON THE STRUCTURAL ENERGETIC PROPERTIES OF ADDITIVELY MANUFACTURED COMPONENTS

2.1 Introduction

As previously discussed, a prelude to this work by Fleck et el. [13] demonstrated the ability to print a multifunctional energetic structural material (MESM); however, characterization of how the material constituents influence the functional capabilities of the components is needed before implementation. Multifunctional energetic structural materials (MESMs) are attractive for many applications in the aerospace and defense sectors, as reactive structures allow for maximum energetic output with the same form factor as compared to inert structural materials [28, 35]. Previous MESM studies have focused on high-density, high-strength materials, such as intermetallic or thermite mixtures, that could act as functional structural elements with highly enthalpic properties. The purpose of these studies was to develop materials suitable for use in projectile systems that could penetrate a target and provide additional enthalpy release upon ignition [28–30]. While the Al/PVDF materials studied in this document do not have the high-density or high-strength capabilities of the previously studied MESMs, the ability to 3D print these materials enables a wide range of previously unachievable applications, specifically in the aerospace and defense sectors, where low density materials are often required.

This section of the document seeks to further the characterization of the structural performance and combustion properties needed for these materials to be used reliably as an MESM. Before significant variations in the AM process are made, this work varies the constituents of the material to gain an understanding of the relationships between its structural and energetic capabilities. This work looks to determine the effect of the Al particle loading and particle size on the structural energetic properties and build material property plots to serve as a guide for designing energetic structures out of Al/PVDF materials.

Varying the material constituents of a metal-fluorpolymer energetic material has been shown to have an effect on the combustion properties of these energetic materials [38–40]. The fuel particle loading can be varied to effectively change the stoichiometry and tune the chemical reaction characteristics of the formulation [41, 42]. The size of the fuel particle is also known to play an important role in the reaction kinetics of metal-fluoropolymer energetic materials, as smaller particle sizes allow for more surface contact with the oxidizing binder [43,44]. In addition to the combustion properties of energetic materials, the same two parameters, particle loading and particle size, are known to have an effect on the mechanical properties of inert, particle-loaded polymer composites. For example, particle loading was shown to have an effect on the modulus of elasticity of silica-epoxy composites, increasing the modulus of the material as more particles were added into the formulation [45]. The ultimate tensile strength had the opposite trend in these materials, decreasing as the particle loading was increased [45]. Increasing the particle size was shown to decrease the tensile strength of several composite materials [46]. While these results give insight as to how the particle loading and particle size may influence the structural energetic qualities of an MESM, these qualities are dependent on the specific constituents and formulations used. Therefore, characterization of the material-process-function relationships is needed for specific MESM formulations before structural elements can be manufactured and integrated at the systems level.

This work looks specifically at seven different formulations, all of which were deemed as feasible candidates for FFF printing. The mechanical properties were determined via the quasi-static tensile testing of 3D printed dogbones. The combustion properties of these formulations were predicted using a thermochemical code, Cheetah 7.0 [47], and quantified via burning rate measurements and DSC analysis. These performance metrics were analyzed in order to gain a better understanding of the relationships between the combustion properties and structural performance of metal-fluoropolymer materials. Property plots were created in order to facilitate rapid visualization of the trade-offs between the mechanical properties and the combustion properties of the seven formulations considered.

2.2 Materials and Methods

2.2.1 Pellet, Filament, and Sample Preparation

A three-step process was used to 3D print dogbones (ASTM D638, Type V [48]) for quasi-static mechanical testing, as well as samples for burning rate characterization. The process involved making pellets, extruding them into a filament, and then printing them using a Makerbot Replicator 2X, as previously demonstrated [13]. The work in this chapter involves varying the constituents of the reactive materials during the pellet making process. A typical batch of pellets consisted of 20 g of material to be loaded into the filament extruder (Filabot Original). The 20 g batches were made in 2 g increments due to process and safety limitations. For each 2 g batch, the appropriate amount of PVDF (Kynar 711, Arkema Chemicals) for the formulation was added to a 8 dram glass vial. To this vial, 5 mL of dimethyl formamide (Anhydrous 99.8%, Sigma Aldrich) and 10 mL of acetone (Sunnyside Specialty Chemicals) were added to dissolve the PVDF. Then, the appropriate amount of aluminum (Al) was added in order to achieve the solids loading (wt%) desired. In order to adequately distribute the Al particles, the vials were mixed for 5 min on a digital sonifying horn (Branson Ultrasonics) at an amplitude of 15%. After mixing, the contents of the vials were poured into an aluminum weighing dish (McMaster, 17805T81) and allowed to dry for at least 48 hr and then cut up into pellets (≈2 mm x ≈2 mm x ≈2 mm). Seven different formulations were prepared for this study. For the first five formulations, the solids loading of the aluminum was varied from 10 wt% to 50 wt% in 10% increments in order to study the effect of particle loading on the mechanical and combustion properties of the energetic material. For the variation of the particle loading study, the particle size of the aluminum was kept constant at 4.5 μm (H3, Valimet). The remaining two formulations involved varying the particle size of Al while keeping the particle loading constant (20 wt%) in order to determine the effect of particle size on the mechanical properties of the energetic material. The two other particle sizes of aluminum were 16 μm and 31 μm (H12 and H30, Valimet). These formulations are summarized in Table 2.1.

Table 2.1.
A summary of the constituent study formulations.

Formulation	**% Al** (wt)	**Avg. Al Particle Diameter** (μm)	**% PVDF** (wt)
1	10	4.5	90
2	20	4.5	80
3	30	4.5	70
4	40	4.5	60
5	50	4.5	50
6	20	16	80
7	20	31	80

Each of the pellet formulations shown in Table 2.1 was extruded using a filament extruder (Filabot Original) in order to obtain a 1.65 mm filament capable of being printed with a Makerbot Replicator 2X. The extruder's temperature was set at 195 °C, well below the 375 °C onset temperature, and the extrusion screw was rotated at a rate of 35 rpm. The set up for the filament extrusion process can be seen below in Figure 2.2.1. The energetic pellets were loaded into the extruder and allowed to extrude for 10 min, after which, a purging compound (Filabot, Low Temperature Purge Compound) was released from the remote controlled hopper into the extruder to remove the energetic material from confined conditions. Diameter control of the filament proved challenging due to the extruder being run remotely. In order to better control the diameter, the extruder was placed at a 40° angle from the table top and a Teflon support was used to guide the filament into a receptacle. A fan was used to cool the filament immediately upon extrusion in order to prevent tension from causing diameter irregularities. Using this set up, the diameter of the nozzle could be varied in order to achieve a consistent filament diameter. In addition to the Al/PVDF filament, an inert PVDF filament was made in order to print dogbones with no particle loading for comparison purposes, as well as for the PVDF rafts used to promote build plate adhesion. The same PVDF formulation, only in pellet form (Kynar 710, Arkema Chemicals),

was loaded into the extruder, under the conditions previously detailed, in order to obtain the inert filament.

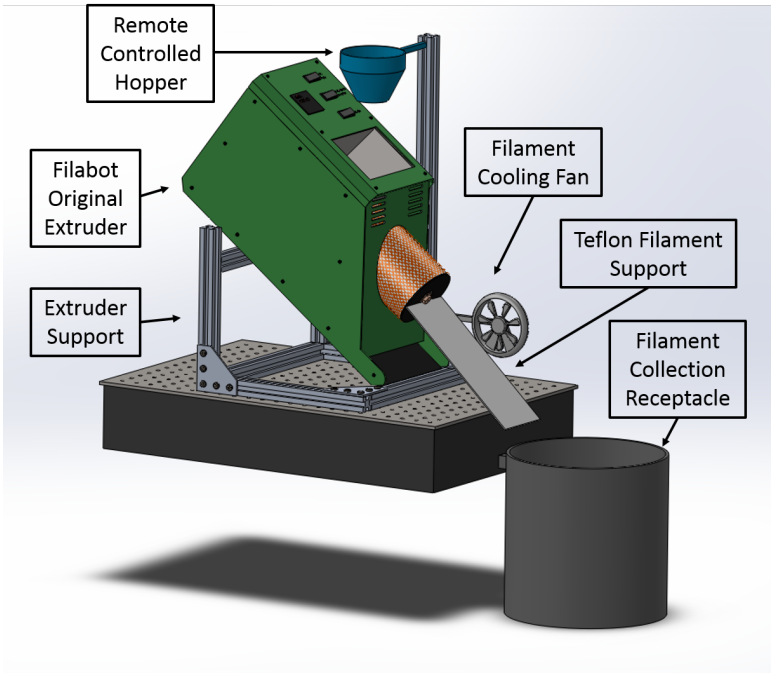

Figure 2.1. Side-view schematic of the filament extrusion process.

The resultant filaments were then printed using a Makerbot Replicator 2X. Print files (.x3g) for the Type V dogbone were prepared using the Simplify 3D slicing software [49]. The dogbones were printed without a shell and with a 0° raster orientation. In order to promote adhesion to the build plate, each dogbone was printed on an inert PVDF (Kynar 710, Arkema Chemicals) raft, which used glue (All Purpose Glue Stick, Elmer's) in order to maintain build plate adhesion. It was determined that if the raft or the glue were not used, significant warping of the dogbones would occur. The important process parameters that were used during printing can be seen in Table 2.2 and an image of the print file with the toolpath for the printer can be seen in Figure 2.2.

Table 2.2.
The important printing parameters.

Parameter	Value	Unit
Nozzle Diameter	0.4	mm
Layer Height	0.2	mm
Shells	0	N/A
Additions	Raft	N/A
Infill Percentage	100	%
Infill Angle Offset	0	°
Extrusion Temperature	230	°C
Bed Temperature	120	°C
Printing Speed	600	mm/min
First Layer Printing Speed	300	mm/min

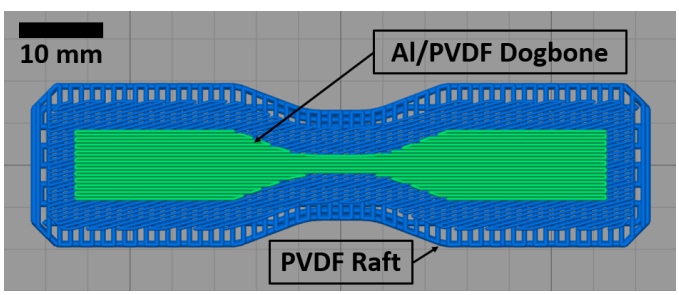

Figure 2.2. The toolpath for the print file of the ASTM D638 Type V Dogbone used for all of the tensile testing.

2.2.2 Mechanical Characterization

In order to characterize the effect of the particle loading (wt% Al), as well as the particle size, on the mechanical properties of the Al/PVDF material, five dogbones (as seen in Figure 2.2) were printed for each of the formulations previously described. These dogbones were used for quasi-static tensile testing purposes with a Mark-10 ESM 1500 Tensile and Compression

Tester [20 μm spatial resolution, 500 N force gauge (0.1% accuracy)]. All of the tensile tests were performed in accordance with ASTM standard D638 [48] in which the dogbone was loaded into 2.54 cm wedge grips (Mark-10, G1061-2) and pulled at a rate of 1 mm/min. The stress was calculated by dividing the load by the cross-sectional area of the neck of the dogbone. The strain was calculated by dividing the elongation by the original length of the dogbone neck. The ultimate strength was identified as the point of maximum stress on the stress versus strain curve. The modulus of elasticity was calculated by using a line-of-best-fit command in MATLAB (The Mathworks Inc.). Figure 2.3 shows a representative stress versus strain curve and identifies how the pertinent values were obtained.

2.2.3 Thermochemical Calculations

In addition to mechanical characterization, thermochemical codes were used to predict the combustion characteristics of the Al-fluoropolymer material. Cheetah 7.0 software was used to calculate the theoretical heat of combustion and adiabatic anaerobic flame temperatures for Formulations 1-5 from Table 2.1 while using the standard heats of formation for the constituents. The heat of combustion was calculated by using the standard Cheetah analysis and represents the total energy output if the formulation were to burn to equilibrium in air at atmospheric pressure. The adiabatic anaerobic flame temperatures were obtained by doing anaerobic rocket calculations and selecting the chamber pressure as atmospheric for the reaction. This should give an approximation to the flame temperature at atmospheric pressure without excess oxygen. This analysis does not take the particle size into account, so Formulations 6 and 7 were not considered for the thermochemical analysis as the results would be the same as Formulation 2. However, it should be noted that it was anticipated that the particle size would affect the combustion performance of the material. This has been well documented in literature for this material system [18, 40]. In order to quantify the effect of the particle size on the combustion performance, as well as verify the trends of the thermochemical code, burning rates and DSC/TGA results were obtained as described in Section 2.2.4.

2.2.4 Combustion Characterization

In order to collect the burning rate measurements, rectangular prisms (2 mm x 2 mm x 75 mm) were printed for all seven formulations in the same manner as the dogbones described previously. These samples were then aligned vertically and mechanically clamped at the bottom. Upon ignition via nichrome wire (Consolidated Electronic Wire and Cable, 24 gauge), videos of the flame propagating down the sample were obtained using a camera (CASIO EX- ZR1000). The camera was operated at a frame rate of 240 fps. An neutral density (ND) filter (THOR Labs, 3.0) was placed between the camera and the sample in order to prevent over exposure. The videos were then processed using an in-house MATLAB script. The flame front was located manually every 10 frames in order to obtain position versus time data. A line of best fit was then used to approximate the propagation speed, or burning rate. Additional combustion characterization was obtained via differential scanning calorimetry (DSC) and thermal gravimetric analysis (TGA), which was performed on all seven formulations using an SDT Q600 (TA Instruments).

2.3 Results and Discussion

Per the procedures previously described, five dog bones of each formulation in Table 2.1 were printed for quasi-static tensile testing. Figure 2.3 shows a representative stress versus strain curve obtained from the tensile tests labeled with the ultimate strength and the line-of-best-fit over the elastic region of the material. The ultimate strength was identified as the point of maximum stress on the stress versus strain curve. The modulus of elasticity was obtained from the slope of the line-of-best-fit. The ultimate strength and modulus of elasticity were obtained from each of the 35 dogbones (5 for each formulation) and are plotted in this section as a function of solids loading and particle size.

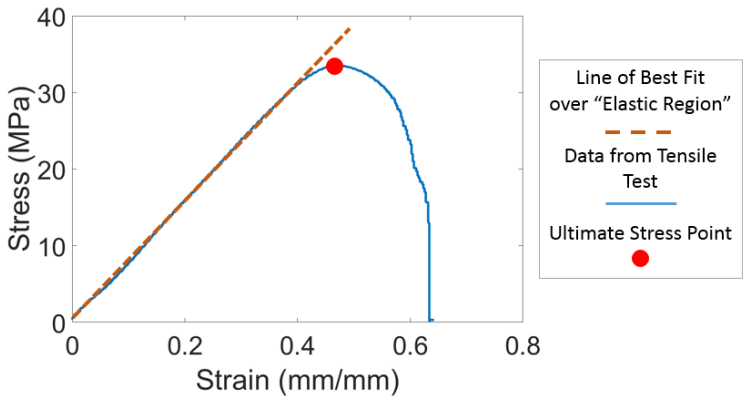

Figure 2.3. Stress versus strain curve for a representative dogbone with the ultimate strength and line-of-best fit labeled. The ultimate strength was identified as the maximum point of stress on the curve. The modulus of elasticity was identified as the slope of the line-of-best-fit.

2.3.1 Effect of Al Solids Loading on the Structural Energetic Properties of Al/PVDF

Effects of Solids Loading on the Mechanical Properties

Of the mechanical properties considered, the modulus of elasticity and the ultimate strength can be seen in Figure 2.4 as a function of the solids loading (wt% Al in the formulation).

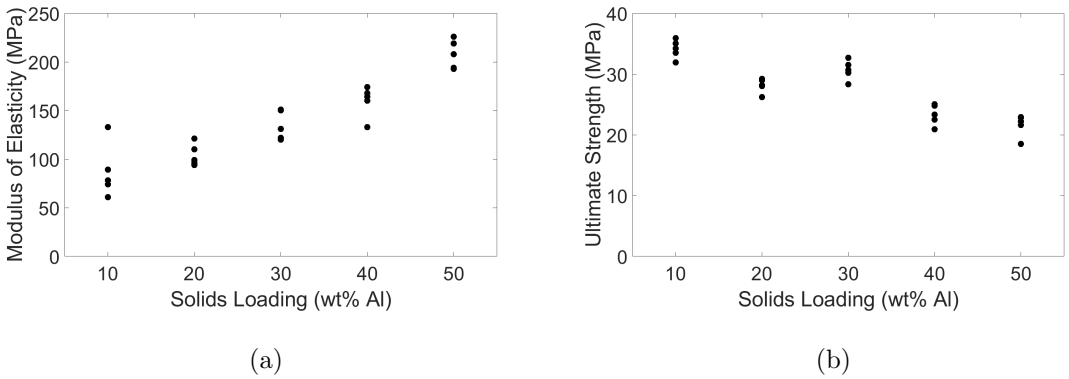

Figure 2.4. Plots showing how the (a) modulus of elasticity and the (b) ultimate strength for the Al/PVDF material are affected as the solids loading is increased.

From these plots, it can be seen that as the particle loading was increased, the modulus of elasticity increased from 71 MPa to 208 MPa when transitioning from a 10% Al loading to a 50% Al loading. The ultimate strength decreased consistently over the same Al loading range, transitioning from 34.5 MPa to 21.6 MPa, approximately a 37% reduction. It should also be noted that as the particle loading was increased, the effective density of these materials also increased. As previously discussed, these light-weight MESMs could be used in a variety of aerospace and defense applications. In these contexts, the weight of the structure is typically crucial. When varying the particle loading in order to optimize the structural performance of these materials, one must also consider the change in density. For the specific Al/PVDF formulations considered in this paper, the densities of the polymer (1.78 g/mL) and metal particle (2.7 g/mL) are similar enough to only cause a 16% increase in effective density when going from a 10% solids loading to a 50% solids loading. For this reason, density was not considered to be of significant importance in this study. However, density should be considered if lower density polymers or higher density particles are utilized.

Effects of Solids Loading on the Combustion Properties

Another category of metrics that should be used to evaluate structural energetic materials are the combustion properties of the material. In an attempt to predict the combustion

performance of these materials, the heat of combustion and adiabatic flame temperature were calculated using a thermochemical code (Cheetah 7.0 [47]). Both of these values are plotted as a function of particle loading in Figure 2.5. The heat (or enthalpy) of combustion represents the potential energy release available for the given formulation. The equilibrium adiabatic flame temperature represents the maximum temperature achieved without heat loss.

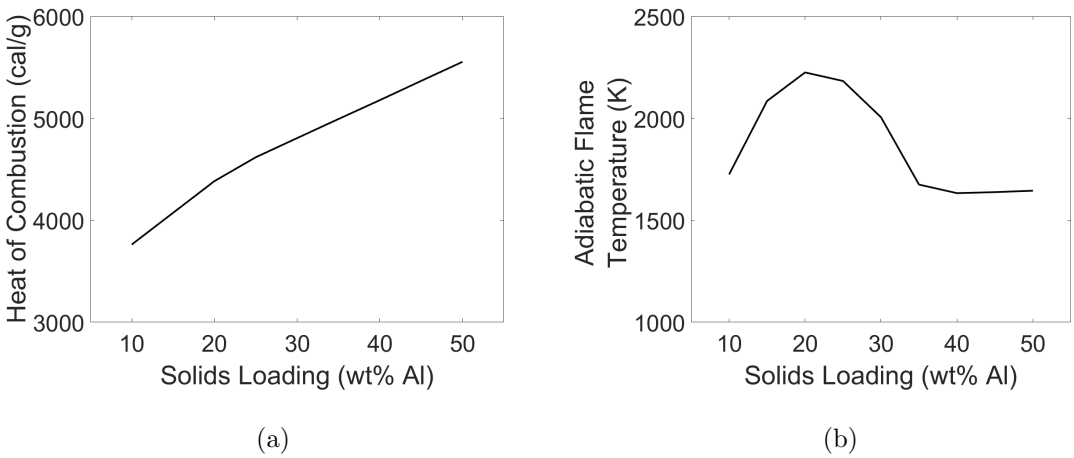

Figure 2.5. Plots showing how the (a) heat of combustion and the (b) adiabatic flame temperature for the Al/PVDF material are affected as the solids loading is increased.

From these plots it can be seen that the total available energy, or heat of combustion, increases as the amount of aluminum in the formulation is increased. This makes intuitive sense as the available chemical energy from the Al is higher than PVDF in air. Thermochemical codes assume the ideal combustion of all of the reactants in air (for the heat of combustion metric), meaning that the maximum available energy possible from the formulation is utilized and equilibrium is achieved. The adiabatic flame temperature shows a peak near 20% Al. This aligns near the "stoichiometric" ratio ($\approx$ 23 wt% Al) of aluminum to PVDF seen in the assumed chemical reaction formula for the material:

$$2\mathrm{Al} + 3\mathrm{C_2H_2F_2} \rightarrow 2\mathrm{AlF_3} + 6\mathrm{C} + 3\mathrm{H_2}. \tag{2.1}$$

In order to confirm that these thermochemical codes could predict the combustion performance of these 3D printed materials, the burning rates shown in Figure 2.6(a) were measured. When comparing the burning rate results shown in Figure 2.6(a) with the flame temperature results in Figure 2.5(b), it can be seen that there is a correlation. For this energetic material system, it is expected that the burning rate will be thermally driven [34]. Figure 2.6(a) shows a peak in the burning rates just above the stoichiometric conditions for this material system, near 30 wt% Al. This peak occurs at a slightly more fuel rich condition as compared to the peak in flame temperature shown in Figure 2.5(b). It should also be noted that if the Al particle content was too low (>10 wt%), the material could not sustain a reaction for the sample sizes considered in these tests. Figure 2.6(a) shows a burning rate of 0 mm/s for Formulation 1. This represents the fact that upon ignition, the flame propagated partially through the sample but eventually quenched and was not able to achieve self-propagation. In addition to the burning rates, Figure 2.6(b) shows results of the DSC analysis for Formulations 1-5. For this analysis, the peaks of the main exotherm were examined, which are highlighted by the arrows. As the reaction kinetics of the material increase, a sharper peak in the main exotherm will be observed. From these plots, it can be seen that the maximum heat flow achieved by each formulation was correlative with the burning rate of the material. This confirms that the slightly fuel rich formulation of 30 wt% Al resulted in the fastest reaction kinetics.

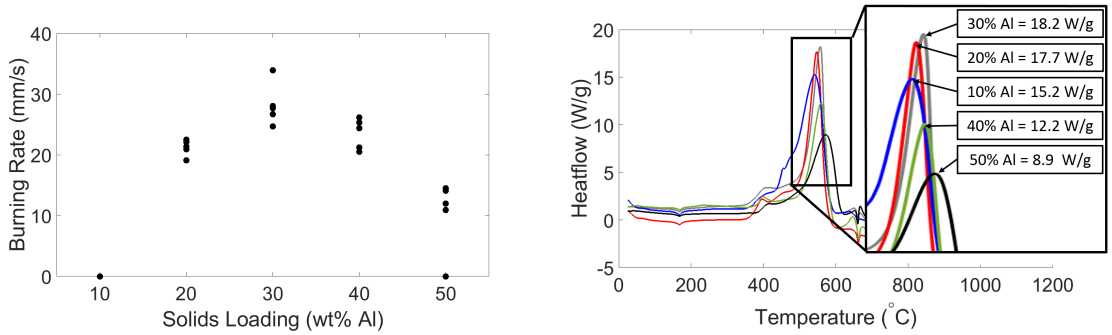

(a) (b)

Figure 2.6. Plots showing how the (a) burning rate and the (b) DSC analysis for the 3D printed Al/PVDF material are affected as the solids loading is increased.

Material Selection Plots for Al/PVDF Structural Energetic Materials

From the plots previously discussed, it can be seen that there are a variety of important parameters to consider when one is looking to optimize the structural energetic performance of a metal-fluoropolymer material. Before considering the size of the metal particle, a variance of the particle loading alone caused many trade-offs when considering the materials' structural energetic properties. Within the mechanical properties, there was a trade off between the strength of the material and the modulus of the material. Within the combustion properties, there was a trade-off between the energy release in air and the burning rate of the material. The purpose of this section is to formulate material selection charts that may be useful during the design phase of these structures. When considering the desired structural energetic performance, these plots can be referenced in order to gain an understanding of the trade-offs between the design criteria. Of all of the possible combinations of structural energetic properties, the most relevant are shown in Figure 2.7.

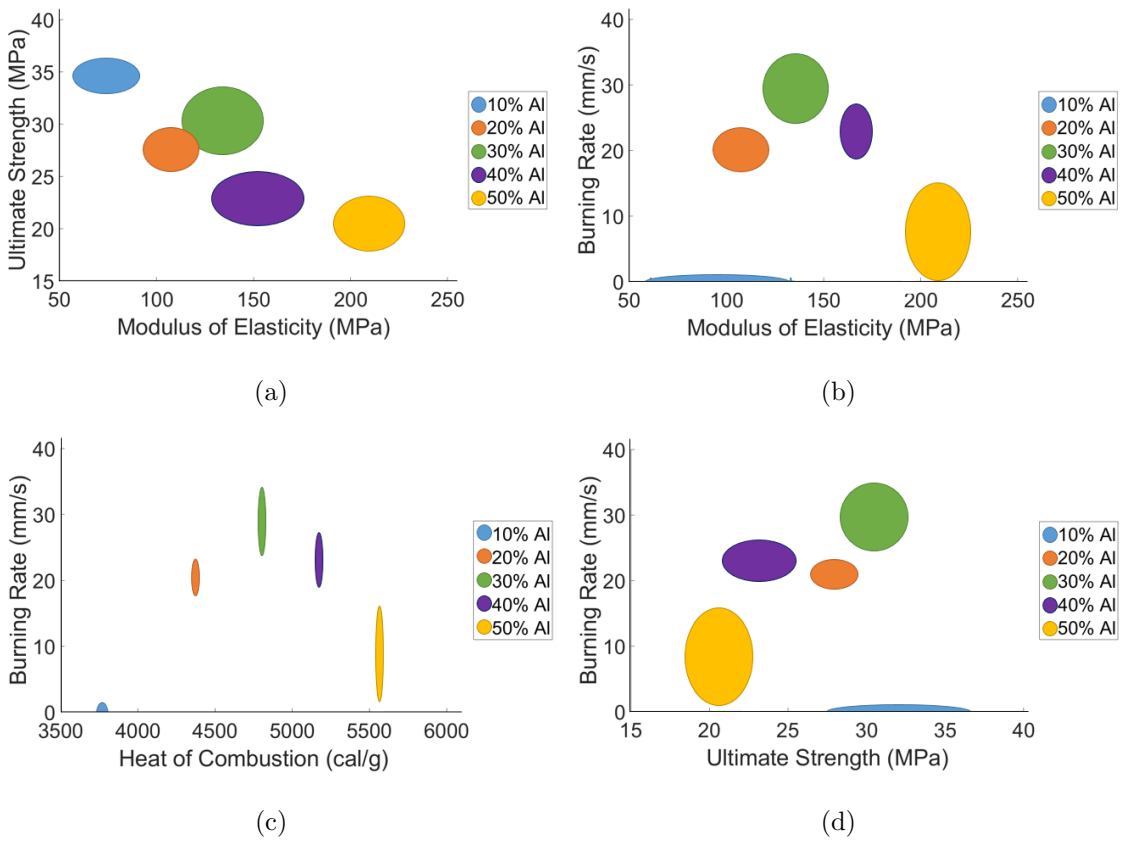

Figure 2.7. Property plots showing the trade-offs between the (a) ultimate strength and modulus of elasticity, (b) burning rate and modulus of elasticity, (c) burning rate and heat of combustion, and (d) burning rate and ultimate strength.

Figure 2.7(a) shows the ultimate strength plotted against the modulus of elasticity. As previously mentioned, it can be seen there was a significant trade off between these two material properties, with no specific formulation having a relatively high strength and high modulus simultaneously. The same can be seen when comparing the burning rate and the modulus of elasticity, as well as when comparing the burning rate and the heat of combustion, as shown in Figures 2.7(b) and 2.7(c) respectively. While the metrics depicted in these three plots are relevant in the design on structural energetic materials, it can be seen that there was no specific formulation that performed best amongst all of these metrics. Based on this, the intended application would determine which formulation was optimally suited for the task. However, a material selection plot that showed a meaningful trend can be seen in

Figure 2.7(d), which compares the burning rate and the ultimate strength of the material. As these two properties highlight the two main functions of this structural energetic, it should be noted that 30% Al formulation had the best combination of burning rate and strength among the formulations considered.

2.3.2 Effects of Al Particle Size on the Structural Energetic Properties of Al/PVDF

In addition to the solids loading in the Al/PVDF formulation, the size of the Al particles was also varied. While changing the particle size is not relevant to the thermochemical calculations, it is known that reducing the particle size can increase the effective kinetics of the reaction due to the reduction of the diffusion scale and increased surface interactions. Because of this, the Al particle size was varied over a range that would be viable for lightweight MESMs. As there is significant inherent risk during processing and handling with nanoscale Al particles, only particle diameters of 4.5 μm and above were considered. The same process was used in order to determine how the particle size affects both the mechanical properties, as well as the combustion performance. First, the mechanical properties were determined. Figures 2.8(a) and 2.8(b) show the modulus of elasticity and the ultimate strength for the Al/PVDF materials as a function of the particle size. From these plots, it can be seen that no significant trend was seen in either the modulus of elasticity or the ultimate strength over the range of the particle diameters considered. When comparing Figure 2.8 with Figure 2.4, the mechanical properties varied much more as a function of the particle loading rather than the particle size for the formulations considered.

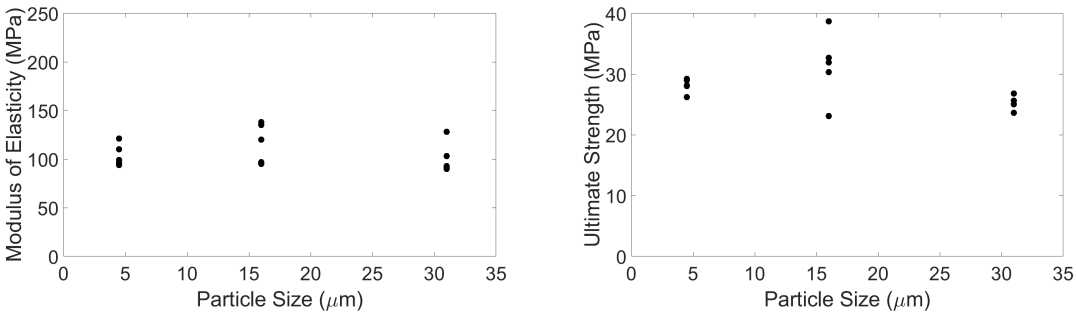

(a) (b)

Figure 2.8. Plots showing how the (a) modulus of elasticity and the (b) ultimate strength for the Al/PVDF material are affected as the Al particle size is increased.

Particle sizes above ≈30 μm were not considered due to their inability to act as a viable fuel for these Al/PVDF energetic materials. This was determined by the acquisition of burning rates for Formulations 2, 6, and 7, which can be seen in Figure 2.9(a). From this plot, it can be seen that as the particle sized was raised, the burning rate of the material went down (holding the solids loading constant at 20 wt% Al). This trend was expected as the smaller particle sizes increase the effective surface area for the fuel to react with the oxidizer. For Formulation 7, once ignition was achieved, the flame front was quenched for the burning rate samples. It should be noted that larger sample sizes were able to sustain a self-propagating flame. However, in order for a structural energetic to be viable, propagation for small features sizes is vital. For this reason, particle sizes above ≈30 μm were not considered. The DSC results shown in Figure 2.9(b) confirm these results.

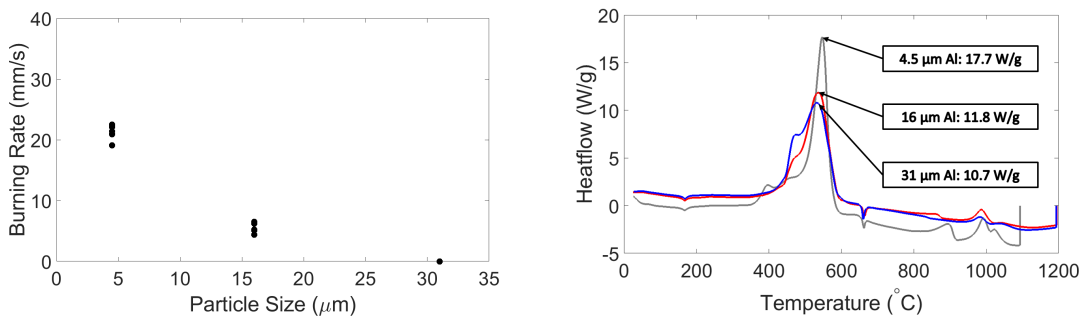

(a) (b)

Figure 2.9. Plots showing how the (a) burning rate and the (b) DSC analysis for the 3D printed Al/PVDF material are affected as the particle size is increased.

2.4 Conclusions

The constituents of an Al/PVDF MESM were varied in order to determine the effect of solids loading and particle size on the mechanical and combustion properties of the material. The mechanical properties considered were the modulus of elasticity and the ultimate strength, both determined from the quasi-static tensile testing of 3D printed dogbones. As the solids loading was increased, the modulus of elasticity increased, while there was a reduction in the ultimate strength. The combustion characteristics of heat of combustion and adiabatic flame temperature were determined as a function of solids loading using a thermochemical code, Cheetah 7.0. The heat of combustion showed a constant increase when transitioning from a 10% solids loading to a 50% solids loading. The adiabatic flame temperature showed a peak at the 20% solids loading formulation, which is near stoichiometric conditions for the Al/PVDF material. In order to experimentally quantify the combustion performance of the seven formulations considered, burning rates were obtained and DSC/TGA analysis was conducted. The burning rates showed a correlation with the adiabatic flame temperatures obtained from the thermochemical codes, showing a peak at slightly fuel rich conditions. Both the modulus of elasticity and the ultimate strength were shown to not be significantly affected by the particle size over the range of diameters considered. However, the burning rate results showed that as the particle size was increased, the combustion

performance decreased significantly. The trends obtained for the specific Al/PVDF formulations considered give insight into some of the trade-offs in structural energetic performance that can be expected for metal-fluoropolymer energetic materials systems.

3. INFLUENCE OF PRINTING PARAMETERS ON THE STRUCTURAL ENERGETIC PROPERTIES OF ADDITIVELY MANUFACTURED COMPONENTS

3.1 Introduction

The energetic capabilities of the Al/PVDF material have been extensively studied, and its viability to act as a structural element was demonstrated in the previous chapter. However, while the effect of the material constituents is well understood, an investigation into how the AM process affects the functionality of these materials is yet to be completed. The work in this chapter seeks to determine the influence of 3D printing process parameters on the Al/PVDF material's structural energetic properties. The effect that various printing parameters have on the structural integrity of 3D printed components has been well studied, identifying print direction, or raster orientation, as one of the most significant. Previous studies showed that the significance of print direction varies by material, so this provides a logical first step as to what to characterize first. In order to quantify the effect of print direction on the structural properties of Al/PVDF, dogbones and burning rate samples, similar to those described in Chapter 2, were printed with multiple raster orientations. The dogbones were also printed with and without aluminum in order to more accurately compare to a standard 3D printing material (ABS) that was not particle loaded. In addition to determining the effect of print direction on the mechanical properties and burning rates of Al/PVDF, two truss samples were printed to simulate realistic structural elements. These trusses demonstrated the ability to tune the structural properties of the material during the design process and were then burned in order to demonstrate the energetic functionality of the MESM.

3.2 Methods and Materials

In order to investigate the effect of print direction, a similar three-part process to that described in Chapter 2 was used to print dogbones (ASTM D638, Type V [48]), truss designs (ASTM standard D7264 [50]), and burning rate characterization samples. The filaments for the inert-PVDF material as well as the 20 wt% Al/PVDF material used in this section were made using the procedure described in Section 2.2.

3.2.1 Sample Preparation

Three types of samples were prepared for the experimentation detailed in this chapter in order to investigate the dependence of the structural energetic properties of the Al/PVDF material on the raster orientation of the samples. The first was the same dogbone (ASTM D638, Type V [48]) used in Chapter 2 which was used for tensile testing purposes to determine the modulus of elasticity and ultimate strength of the material. For each material, 5 dogbones were printed with a 0° print direction and 5 were printed with a 90° print direction in order to determine the effect of the bead orientation on the mechanical properties of the 3D printed FFF components. Figure 3.1(a) and Figure 3.1(b) show the 0° extrusion path and the 90° extrusion path respectively. Other than the print direction, all of the printing parameters were held constant and are summarized in Section 2.2.

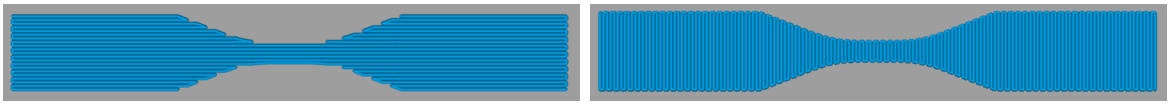

(a) (b)

Figure 3.1. Extrusion path for a single layer of the (a) 0° print direction samples and the (b) 90° print direction samples.

The next sample was a simple bar (detailed in Chapter 2) to be used for burning rate measurement purposes. Once again, 5 samples of the Al/PVDF material were printed in

the 0° and 90° print direction in order to determine the effect of the bead orientation on the burning rates of the 3D printed FDM materials.

The last type of sample was a truss design, which was used to simulate an actual structural component, such as a sandwich panel or a support element. These trusses were designed in reference to ASTM standard D7264 [50] with two different internal structures (designated as A and B), which can be seen in Figure 3.2(a) and Figure 3.2(b), respectively. The two different internal designs were selected to simulate components with similar weights and print times, but different structural properties.

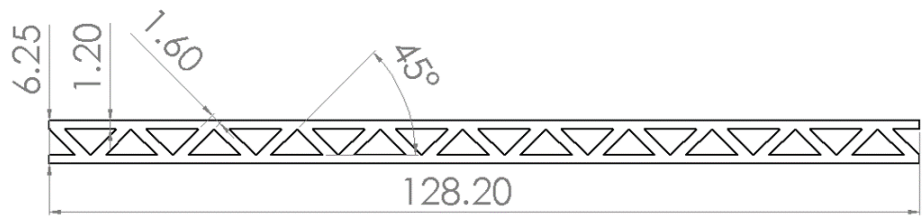

(a)

(b)

Figure 3.2. Truss designs (a) A and (b) B (dimensions in mm) utilized in 3-point bending tests in order to demonstrate the structural qualities of the Al/PVDF material, as well as the ability to adjust effective mechanical properties during the design process.

3.2.2 Sample Characterization

All of the dogbones, as well as burning rate samples, were tested per the procedures laid out in Chapter 2. All of the truss specimens were tested using a 3-point bending apparatus (Mark-10, G1096) in accordance with ASTM standard D7264 [50] with a span of 100 mm

Table 3.1.
A summary of the tensile test results.

	0° Print Direction		**90° Print Direction**	
Material	PVDF	Al/PVDF	PVDF	Al/PVDF
Modulus of Elasticity (MPa)	118 ± 15.6%	104 ± 16.3%	97 ± 10.2%	79 ± 18.4%
Ultimate Strength (MPa)	39.6 ± 5.3%	28.1 ± 6.7%	37.7 ± 7.3%	25.8 ± 7.6%

between the supports. The force from the nose was applied midspan at a rate of 1 mm/min. The load and displacement data for the 3-point bending tests were then converted into flexural stress and strain per ASTM standard D7264 (Procedure A) to obtain the stress versus strain curves seen in the following section.

3.3 Results and Discussion

3.3.1 Tensile Tests

In order to determine the effect of the particle loading on the mechanical properties of the material, inert (PVDF only) dogbones were printed in addition to the Al/PVDF dogbones (20 wt% Al). In order to determine the effect of the print direction on the mechanical properties, the dogbones were also printed in two separate orientations as shown in Figure 3.1. Figure 3.3 shows four stress versus strain plots for each variation of the sample set described. The ultimate stress, as well as the modulus of elasticity, was recorded for each sample (these results are summarized in Table 3.1 along with the average for each sample type ($n = 5$) with the maximum deviation from mean.

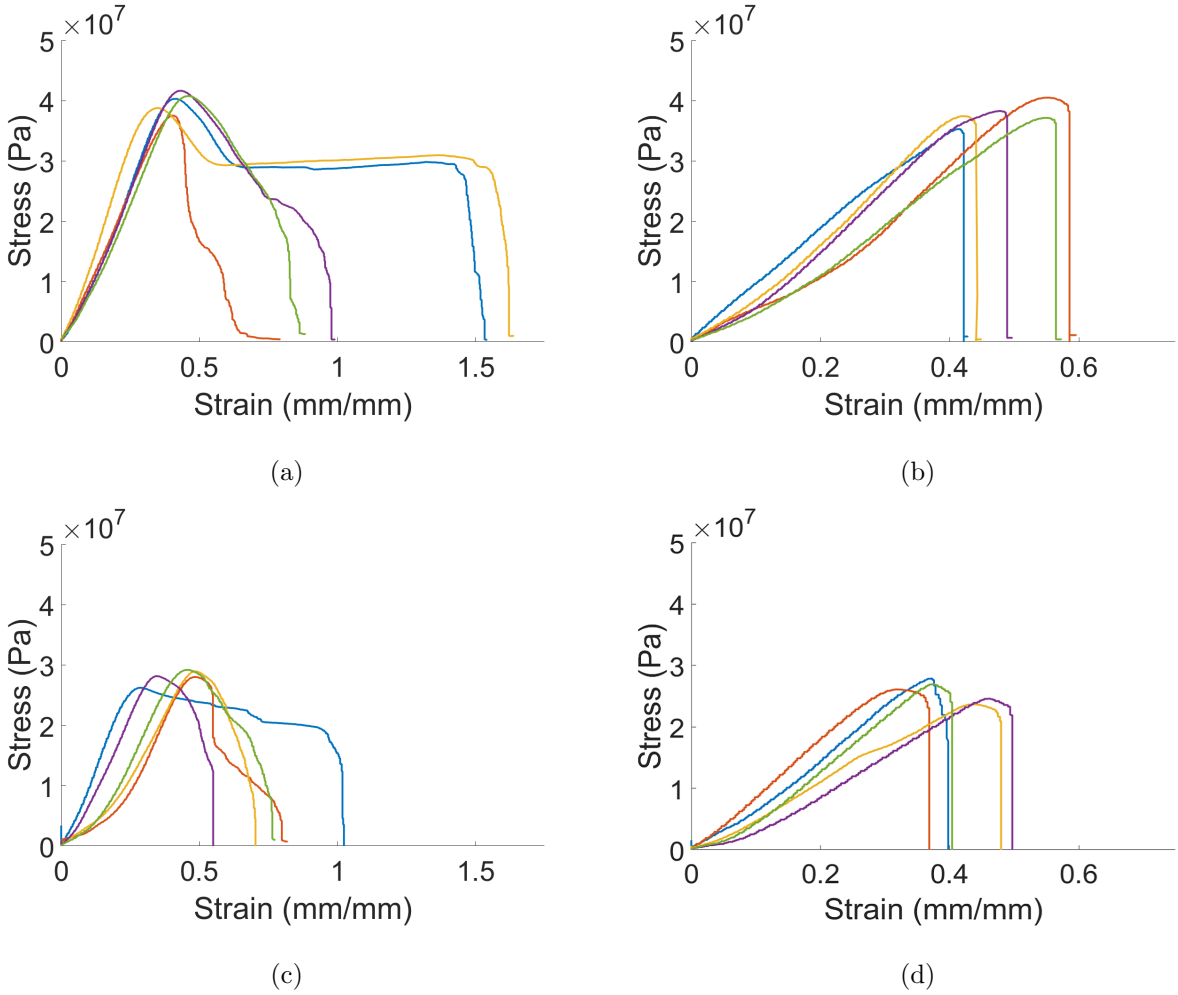

Figure 3.3. Stress versus strain plots for (a) PVDF dogbones with a print direction of 0°, (b) PVDF dogbones with a print direction of 90°, (c) Al/PVDF dogbones with a print direction of 0°, and (d) Al/PVDF dogbones with a print direction of 90°.

From Table 3.1, it can be seen that there was more variance in the modulus of elasticity across all of the samples than in the ultimate strength. Baseline tests were performed using acrylonitrile butadiene styrene (ABS) filaments (Makerbot, red), one of the most common and well characterized FDM materials, in order to determine what variances should be expected. The maximum deviations displayed in Table 3.1 were shown to be comparable to the baseline tests and therefore deemed acceptable. While deviations in the modulus of elasticity were greater than those seen in the ultimate strength, the increase in deviation was attributed mostly to the simplicity of the calculation method described in Section 2.2.2, in which the slope of the line of best fit through the linear section of stress verses stain data was used.

When considering the effect of the particle loading on the mechanical properties of the material, it was found that the ultimate strength was reduced by approximately 30% when going from a 0% to a 20% particle loading by mass, regardless of the print direction. A similar trend was also seen in the modulus of elasticity, where it decreased approximately 15% for both print directions when the sample was particle loaded. However, while the ultimate strength was reduced upon the addition of the Al particles in order to make the material energetic, the mechanical properties were still comparable to the ABS baseline material mentioned previously. This result proved that the Al/PVDF material, regardless of print direction, was comparable to ABS in terms of structural integrity and is a viable material for printing energetic structural elements.

When considering the effect of the print direction on the mechanical properties, it was found that a 0° orientation resulted in the highest modulus of elasticity and the highest ultimate strength, regardless of the particle loading. The modulus of elasticity decreased approximately 20% when going from a 0° print direction to a 90° print direction. The ultimate strength was shown to be less affected by the print direction, with only a 5% reduction when transitioning between a 0° to a 90° print direction. It should also be noted that raster orientation affected the failure mode of the specimen. This can be seen in Figure 3.3 where the 0° samples resulted in larger strains at which failure occurred. This effect can be observed in Figure 3.4, where the 0° samples tended to neck whereas the 90° tended to fail in a manner similar to a fracture. The necking behavior seen in the 0°

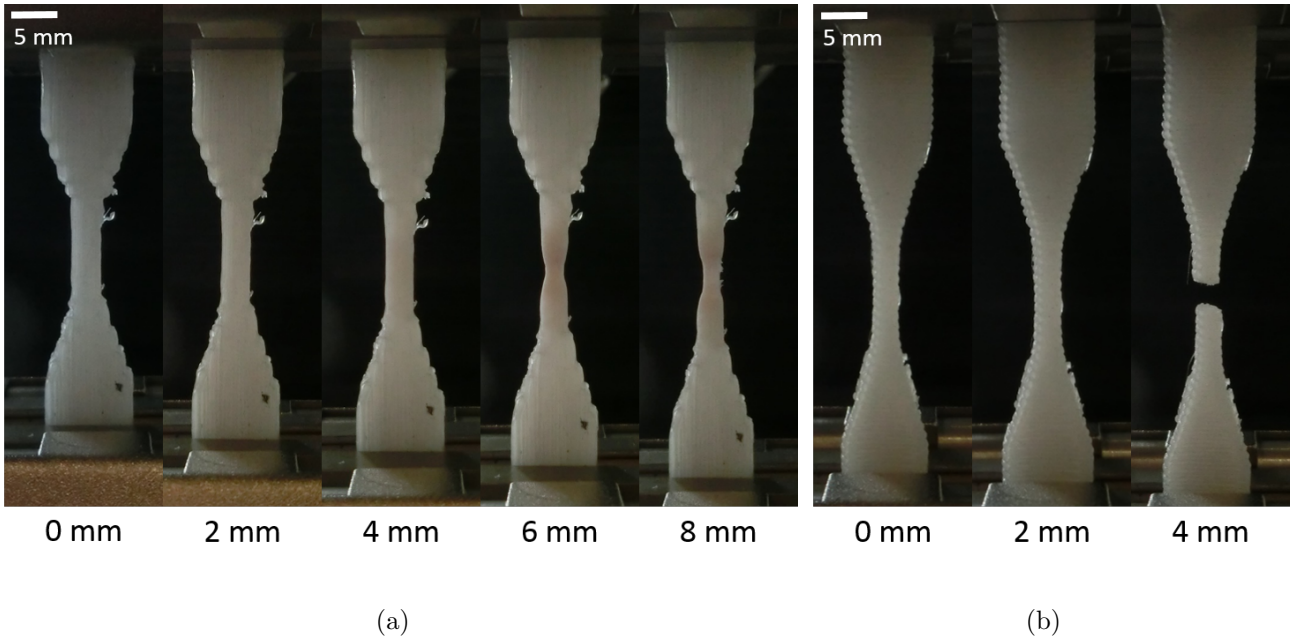

Figure 3.4. A progression of a tensile test for a (a) 0° PVDF specimen and a (b) 90° PVDF specimen with elongation values below each frame.

specimens is typical failure behavior for polymers. However, the fracturing behavior seen in the 90° samples indicates that the effects of the bead-to-bead adhesion of the material are dominating the failure event. The failure surfaces in the neck of the dogbones were imaged under a microscope in order to compare the failure mechanism of each print direction. The 0° sample showed evidence that the individual print beads necked individually. The 90° sample showed that the crack propagated cleanly along the interface of two adjacent print beads. Due to the uneven nature of the failure surface, clear images of the entire surface were difficult to obtain under the microscope and therefore were not included in this document. Overall, the fundamental difference in the failure mechanisms needs to be taken into account when designing FDM structural elements. In practice, one must consider the load direction and whether or not a rapid failure event is acceptable or desirable.

3.3.2 Burning Rate Dependence on Print Direction

The burning rate samples described in Section 2.2.4 were prepared in order to determine the effect of the print direction on the burning rate of the material. Five samples were printed for each print direction, and high speed videos of the deflagration events were recorded and analyzed to obtain flame front position verses time data. A sub-selection of still frames of a representative deflagration event with the corresponding flame front position versus time plot can be seen in Figure 3.5. The burning rates were obtained from the slope of a line of best fit [as shown in Figure 3.5(b)] and the results are summarized in Table 3.2. The samples were found to have comparable burn rates, with no distinguishable difference between the 0° orientation burn rates and the 90° orientation burn rates, which had an average of 21.6 mm/s across all of the samples and a maximum deviation of 2.8 mm/s. Deviations from the mean were consistent for both sample sets. Accordingly, it was concluded that the print direction does not need to be taken into account when considering combustion performance for the conditions considered.

Table 3.2.
A summary of the burning rate measurements.

Sample Set	Burn Rate (mm/s)	Max. Dev. (mm/s)
0° Print Direction	21.14	2.05
90° Print Direction	22.12	3.31
Total Sample Set	21.63	2.82

3.3.3 3-Point Bending Tests of Al/PVDF Trusses

The trusses shown in Figure 3.2 were tested in a 3-point bending apparatus in order to demonstrate the ability to adjust the internal structural geometry, and therefore the overall structural properties of the material, on the fly. The trusses were designed to have the same

(a)

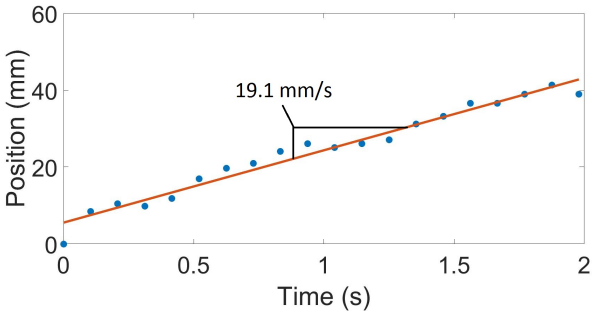

(b)

Figure 3.5. (a) Still frames in 0.5 s increments from a video of the deflagration of a 90° burning rate specimen with (b) the corresponding position verses time graph used to obtain the burning rate.

print times and use the same amount of material, but provide different structural properties. The progression of the 3-point bending for both designs can be seen in Figure 3.6. The flexural stress versus strain curve was calculated for both samples and can be seen in Figure 3.7.

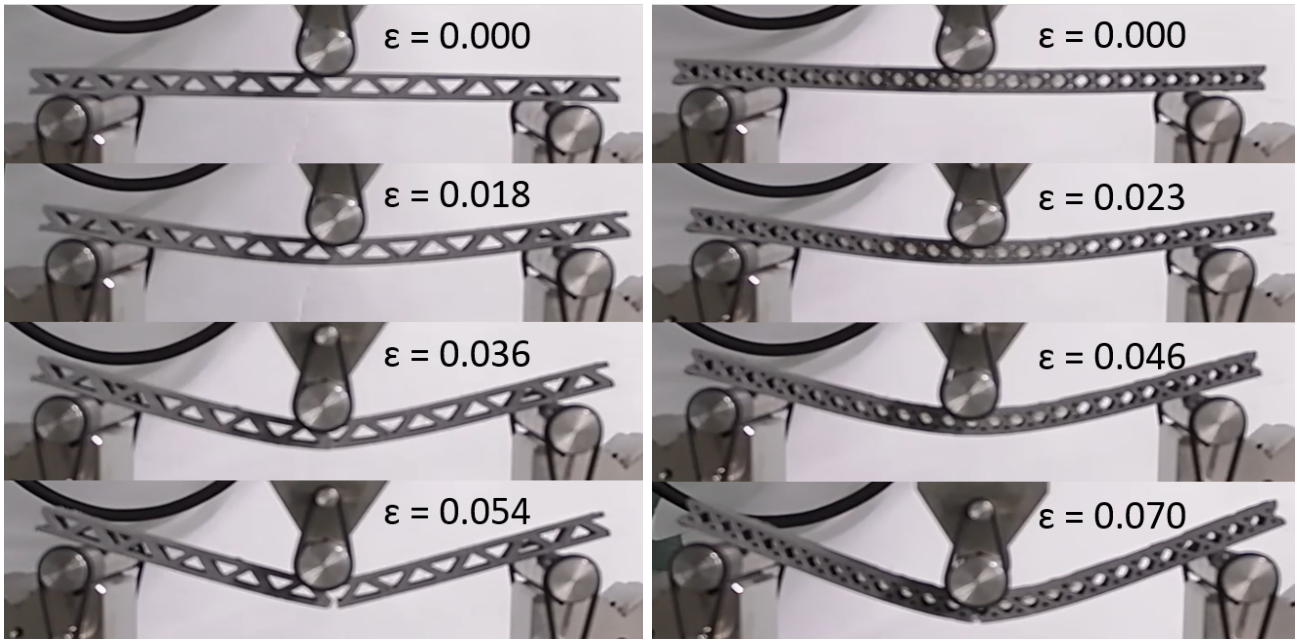

(a) (b)

Figure 3.6. The progression of a 3-point bending test for (a) Al/PVDF Truss A and (b) Al/PVDF Truss B.

From Figure 3.6 and Figure 3.7, it can be seen that the trusses performed differently during the 3-point bending tests. This result demonstrates the potential to control the structural performance of these materials during the design process. To demonstrate the energetic capabilities of the larger structures, Truss B was ignited using Nichrome wire (Consolidated Electronic Wire and Cable, 4 gauge). A video of the deflagration event was obtained using a high-speed camera (BW Phantom Camera V 7.3) with an exposure time of 5 μs and a rate of 100 fps. Still shots from the video can be seen in Figure 3.8.

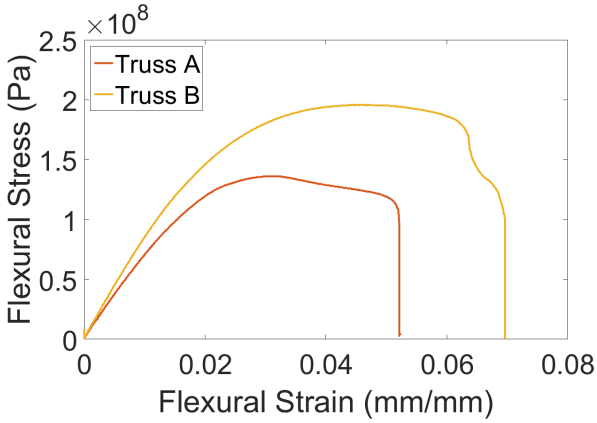

Figure 3.7. Flexural stress versus strain curve for both Truss A and Truss B.

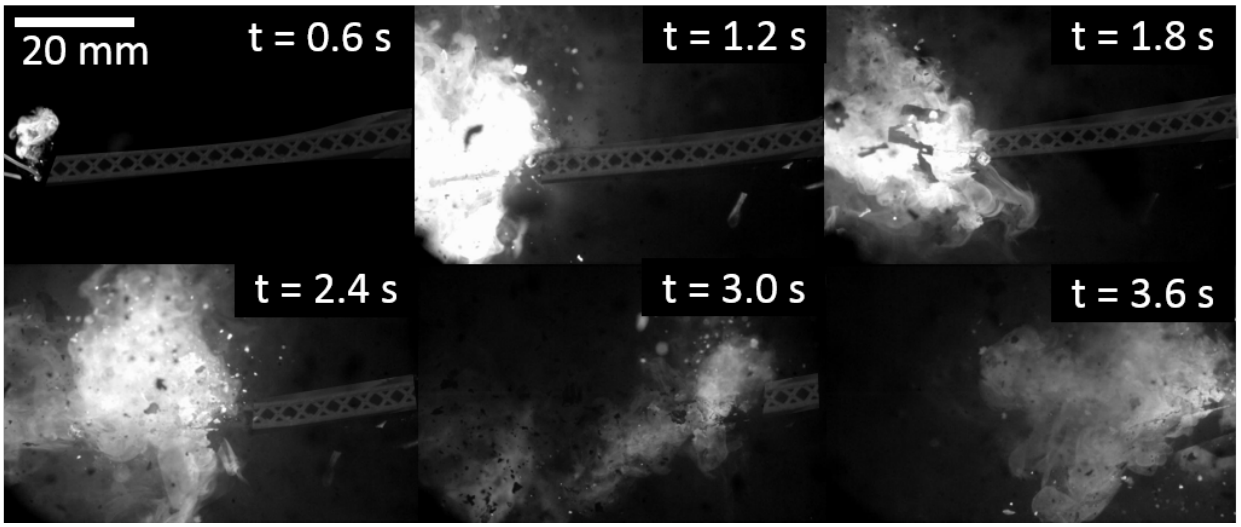

Figure 3.8. Still shots from the deflagration of Truss B obtained using a high speed camera with an original image overlayed to indicate the progression.

3.4 Conclusions

This chapter investigated the effect of print direction on the structural energetic properties of the Al/PVDF material. The modulus of elasticity was found to be dependent on the print direction of the material, reducing from 104 MPa to 79 MPa and 28.1 MPa to 25.8 MPa respectively when transitioning between a 0° print direction to a 90° print direction. The print direction was also shown to have an effect on how the specimen failed, resulting in a necking failure for the 0° specimens and a fracture failure for the 90° specimens. Burning rate measurements were obtained for both print directions, but the results showed that the burning rate had no dependence on the print direction. Truss designs were also printed and burned in order to simulate a realistic structure design. The ability to change the structural properties during the design phase was also demonstrated.

4. THE EFFECT OF INTERLAYER COOLING ON THE MECHANICAL PROPERTIES OF 3D PRINTED ABS STRUCTURES

4.1 Introduction

While the past two chapters have investigated a few of the more obvious parameters that would impact the structural energetic performance of Al/PVDF, many more parameters still need to be explored. Literature indicates that other important FFF process parameters include, but are not limited to, the air gap, layer thickness, number of contours, raster width, and extrusion temperature [51]. Many of these parameters affect the mechanical properties, in some part, due to them having an effect on the layer-to-layer adhesion. While the majority of the work in this document focuses on the additive manufacturing of energetic materials, many of these parameters can be studied on inert materials, in order to mitigate risk. This chapter focuses on experiments conducted with an inert material (ABS). It is believed that the layer-to-layer adhesion issues arise from interlayer cooling, or the amount a layer is allowed to cool before the next layer is deposited. The work in this chapter seeks to quantify the effect that interlayer cooling, which can be affected by numerous printing parameters, has on the mechanical integrity of FFF parts.

During FFF manufacturing, the uneven cooling of deposited material can produce warping, poor layer adhesion, and layer separation [36]. Enclosures are often used around AM machines to prevent heat loss, but interlayer cooling can still occur. The amount of time a layer of material is allowed to cool before the next layer is deposited is an important parameter, since the process of interlayer bonding is thermally driven [36, 37]. Complex part geometries may result in one section of a part being given ample time to cool while another section of the part is printed. In many cases this may be unavoidable, particularly with larger prints. Nonetheless, it is important to understand the implications of interlayer cooling on the final product's material properties. It seems reasonable to assume that poorly adhered layers would produce decreased strength, particularly when the load direction aligns

with the build direction. However, the extent of the effects of interlayer cooling and layer adhesion on the compressive and shear properties of FFF parts, to the best of the author's knowledge, has not been studied.

In order to investigate the effect of interlayer cooling, acrylonitrile butadiene styrene (ABS), a standard FFF material, was used in a Makerbot Replicator 2X to print a true compression (TC) specimen following the ASTM D695-15 [56] standard and a shear compression (SC) specimen following the design shown in [55]. 5 samples of each specimen were printed at each of 5 different interlayer wait times: 0, 5, 10, 15, and 20 s. A 0 s interlayer wait time corresponded to normal printing, where each layer was deposited immediately after the last. For all of the other wait times, the printer's hot end was moved a distance away from the sample where it idled for the specified amount of time before resuming the print. After fabrication, the samples were compressed using a Mark-10 ESM 1500 Tension and Compression Tester in accordance with ASTM D695-15 [56].

4.2 Materials and Methods

In order to test how interlayer cooling affects the compressive properties of FFF parts, two types of samples were designed. The first was intended to measure the mechanical properties of the samples in pure compression. This true compression (TC) sample was cylindrical, 0.5 in (12.7 mm) in diameter, and 1.0 in (25.4 mm) in height as per the ASTM D695-15 standard on the compressive testing of plastics. The second sample was intended to measure the mechanical properties under shear loading. This shear compression (SC) sample followed the design proposed by Rittel et al. [55], as pictured in Figure 4.1(a). As one can see, the same sized cylinder as the true compression sample was used, except with a slot at a 45° angle from the loading direction. At this slot, there was a 0.1 in (2.54 mm) bridge section connecting the top half to the bottom half. Upon compression, the cylinder sheared along the 45° slot.

Samples were prepared for printing using the Simplify3D slicer software [49]. Important printing parameters are summarized in Table 4.1. The samples were oriented vertically, printing from the bottom of the sample to the top of the sample as they are shown in Figure

4.1(a). Due to the increased precision of fusion based machines in the horizontal plane, circles and curves can be produced with greater accuracy in this plane than those oriented vertically. Since dimensional accuracy can be important for cylindrical parts, this orientation was chosen for mechanical testing.

Samples were printed with 100% infill in an attempt to produce the maximum material strength. Furthermore, Croccolo et al. found that increasing the number of contours (shells) around additively manufactured parts led to increased maximum strength and elastic modulus in tensile specimens [54]. In order to avoid this effect during compression testing, the shells were removed completely from the specimens in the slicing software[1]. Finally, beads were set to print in the same direction for all of the layers. This parameter choice was intended to remove the effect of overlapping layers and further isolate the effect of interlayer wait time on the mechanical properties.

All of the samples were printed on a Makerbot Replicator 2X using 1.75 mm red ABS filament (Makerbot). For both the TC and SC specimens, 5 samples each were printed at each of the 5 different interlayer wait times: 0, 5, 10, 15, and 20 s. The 0 s wait time corresponded to printing the specimen normally - after one layer was completed, the sequential layer would be deposited immediately. For all of the other wait times, the printer's extruder head was moved approximately 100 mm away from the specimen and idled there for the specified time at what is referred to hereafter as the stall position. In the context of practical additive manufacturing, this simulates the printer working on another feature of a part that is of sufficient distance from the cylindrical feature, to allow it to cool without interference. This isolates the main issue that this paper investigates: whether interlayer cooling affects the bulk mechanical properties of 3D printed structures.

After preparation, the samples were compressed using a Mark-10 ESM 1500 Tension and Compression Tester, as shown in Figure 4.1. As per ASTM D695-15 [56], the compression rate was set to 1.3 mm/min with a spatial resolution of 20 μm. TC samples were compressed until 90% of the maximum force for the load cell (6.7 kN, 6.7 N resolution) was reached.

[1]After printing the specimens, it was discovered that removing shells in the Simplify3D software resulted in parts that were smaller than intended. The size of the infill was not increased by the software to compensate for the lack of shells. This meant that all of the specimens were about 0.03 in (0.8 mm) smaller in diameter than intended.

This allowed for the collection of data during the elastic deformation, inelastic deformation, and strain hardening of the samples. The SC samples were compressed until failure using a 2.5 kN load cell (2.5 N resolution). In order to plot the stress versus strain curves seen in the next section, simple definitions of stress and strain were used. Stress (σ or τ) was defined as the force applied divided by the area over which it was acting. For the TC samples, this was simply the force due to the compression divided by the cross sectional area of the cylinder. For the SC samples, the force due to compression was projected onto the direction of the 45° slot (to get the component of force causing shear stress). The area used was the thickness of the connecting area (2.54 mm) multiplied by the length of the slot. Strain (ϵ) was defined as the displacement divided by the original dimension of the structure. The moduli for both samples was calculated in MATLAB by using a line-of-best-fit command over the linear region of the stress versus strain curve, which was manually selected by the user.

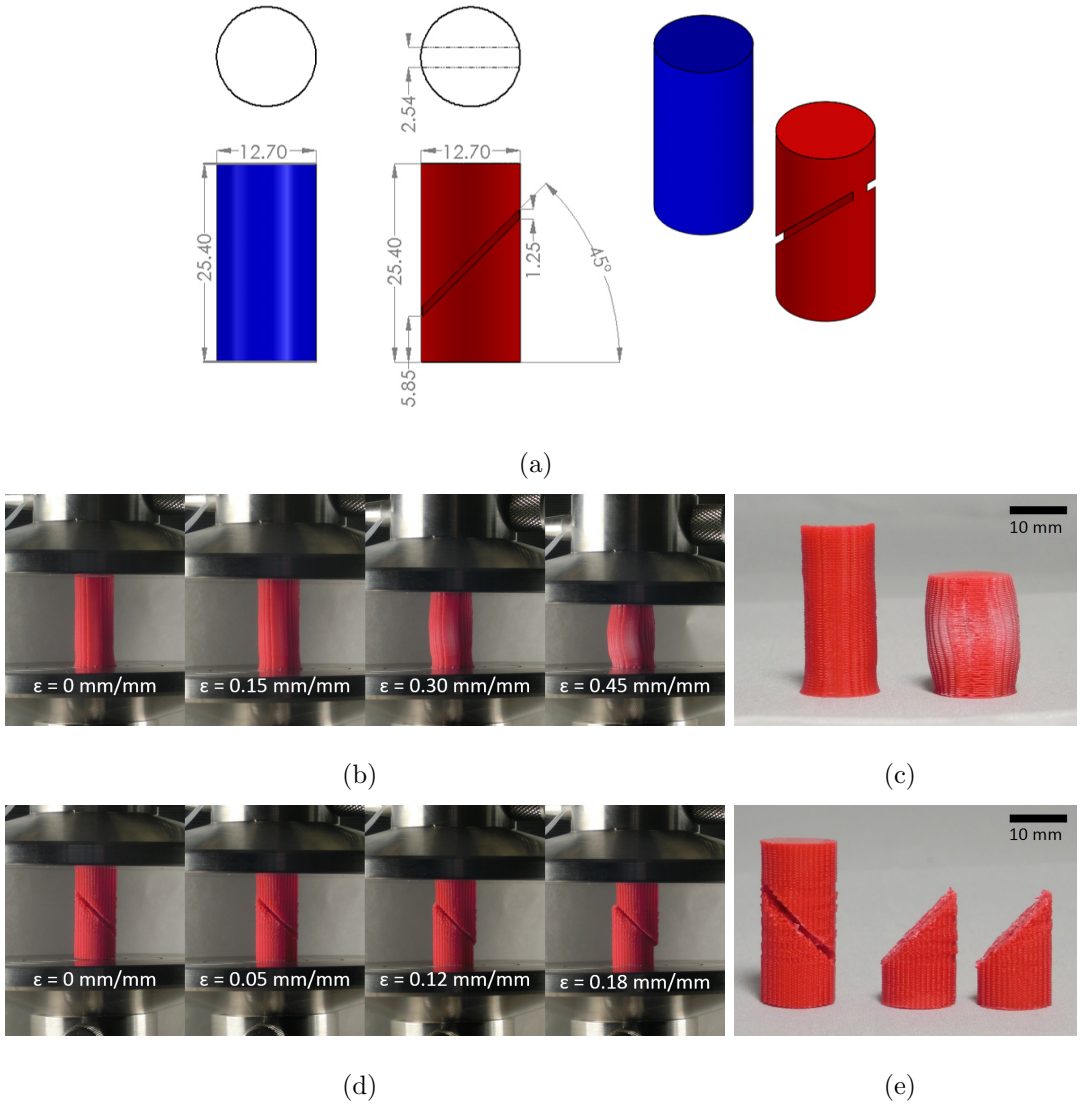

Figure 4.1. (a) (left) True compression and (right) shear compression samples with dimensions in mm. (b) True compression and (d) shear compression testing specimens placed in the Mark-10 ESM 1500 Tension and Compression Tester shown with before and after pictures of each (c and e respectively).

Table 4.1.
The important printing parameters.

Parameter	Value	Unit
Nozzle Diameter	0.4	mm
Extrusion Width	0.4	mm
Extrusion Multiplier	1.00	N/A
Layer Height	0.2	mm
Shells	0	N/A
Fill Percentage	100	%
Extrusion Temperature	210	°C
Bed Temperature	120	°C
Printing Speed	3600	mm/min

4.3 Results and Discussion

Using the methods described above, the following data was collected and processed to produce stress versus strain curves of the FFF parts. Figure 4.2(a) shows the axial compressive stress versus strain curves of the TC specimens. As can be seen, very little variation is present in the compressive moduli between the different wait times. However, a distinct trend can be observed in the yield strength. As the interlayer wait time increased, the yield strength of the TC samples decreased from approximately 39.7 MPa (0 s wait time) to 34.9 MPa (20 s wait time), an approximately 12% decrease. The averages of the modulus of elasticity and the yield strength for the TC samples are plotted in Figure 4.3 as a function of interlayer wait time. These plots show that there is no significant trend observable with the modulus of elasticity as the interlayer wait time was varied, but a trend in the reduction of the yield strength as interlayer wait time is increased can be noticed.

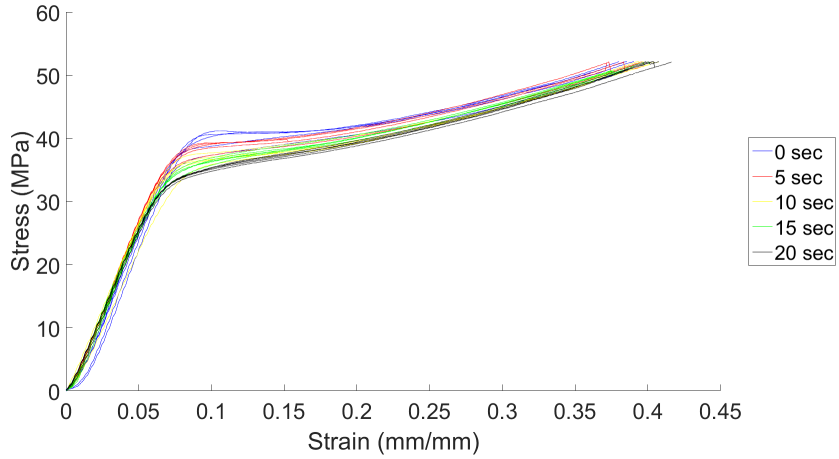

(a)

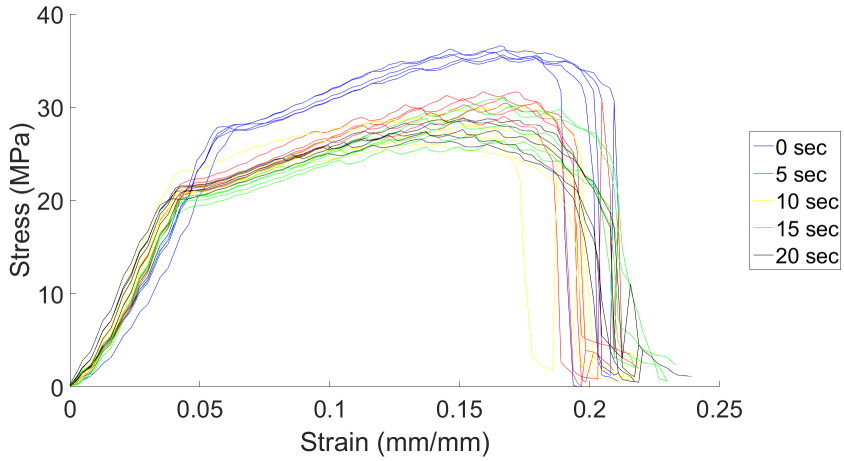

(b)

Figure 4.2. (a) True compression and (b) Shear Compression stress versus strain curves.

All of the TC specimens produced were geometrically identical (i.e. there were no visible defects caused by the dwell times in between the layers). Therefore, it is reasonable to assume that the decrease in yield strength can be attributed to interlayer cooling. Cooling of the ABS in the sample seems to decrease its adhesion to the new ABS deposited by the printhead, which in turn decreases the overall strength of the additively manufactured part. These findings support the hypothesis that the more a layer is allowed to cool before it is bonded with the next layer on top of it, the weaker that bond will be. This result should

be kept in mind when designing and preparing end use FFF parts for production, and may influence the decision of whether or not to use an enclosure or other heating elements during printing.

Figure 4.2(b) shows the shear stress versus strain curves of the SC specimens. The trends seen in the SC samples were similar to the trends seen in the TC sample trends. There is little observable difference in the shear moduli between samples with differing wait times, but a trend can be seen in the yield strength. The yield strength among the samples drops from 28.0 MPa (0 s wait time) to 21.1 MPa (20 s wait time), an approximately 25% decrease. The averages of the shear modulus and the ultimate strength for the SC samples are plotted in Figure 4.3 as a function of interlayer wait time. Once again, there is no trend noticed in the shear modulus data. However, a significant trend is seen in the ultimate strength as the interlayer wait time is increased.

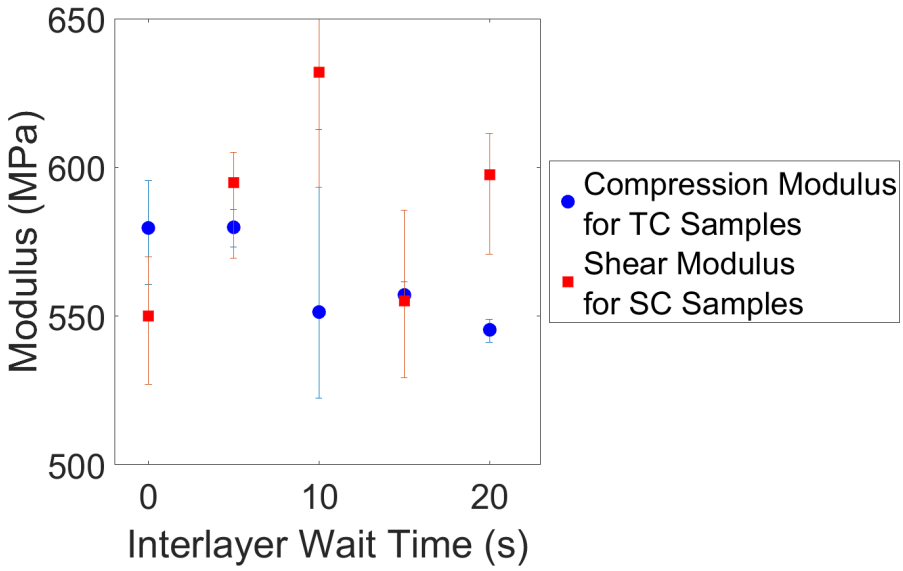

(a)

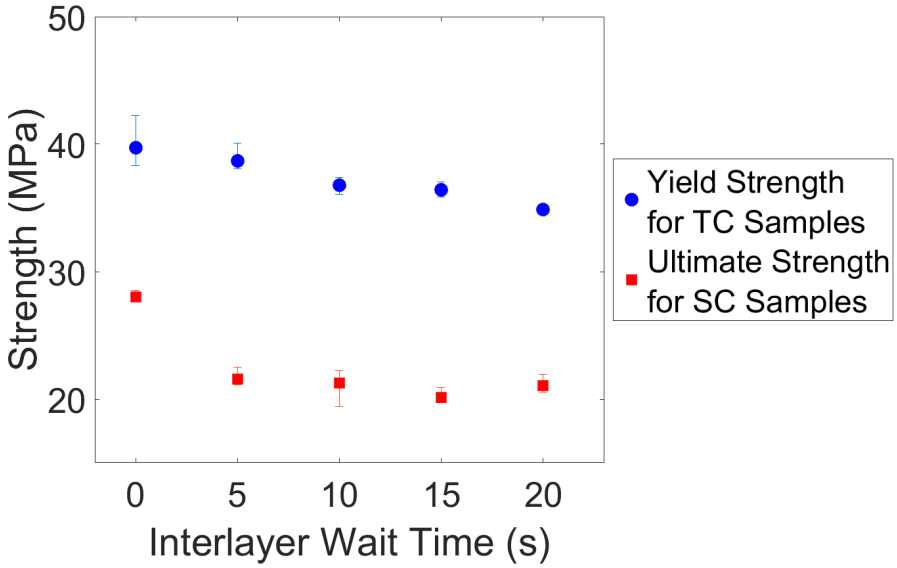

(b)

Figure 4.3. (a) The modulus and (b) strength plotted versus interlayer wait time with error bars representing the minimum and maximum of each set.

Further investigation was completed in an attempt to quantify the rate of the cooling of each layer before the successive layer was printed. Thermal data was collected using a FLIR A655sc thermal camera in order to determine the amount the cooling of the top layer of a

TC sample over the 20 s wait time. Figure 4.4(a) shows the cooling of the hottest point after each layer is printed, along with still frames of a representative layer over the 20 s interlayer wait time. Figure 4.4(b) shows still frames of a representative layer of the printed cylinder cooling down over the 20 s interlayer wait time.

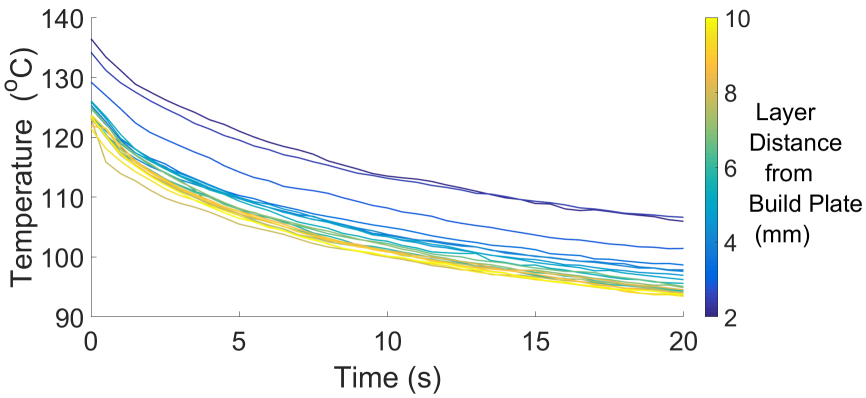

(a)

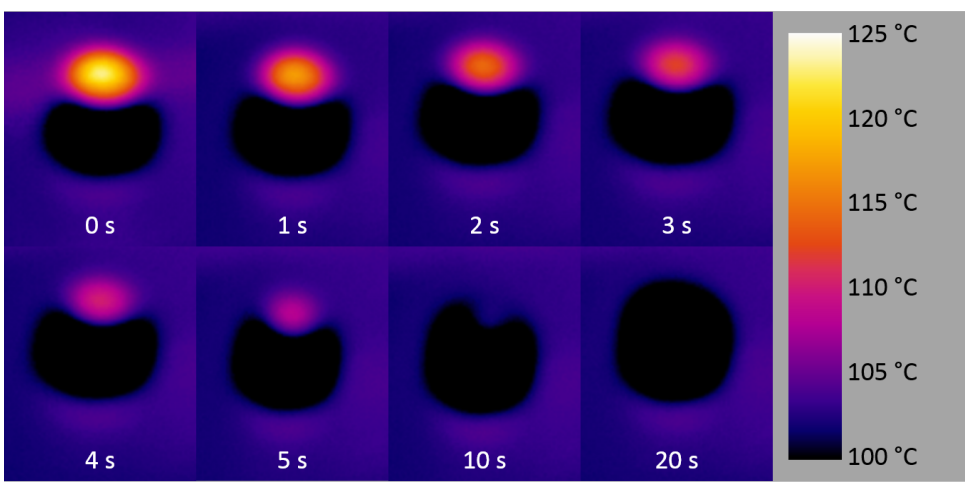

(b)

Figure 4.4. (a) Temperature versus time plot of the hottest pixel for multiple layers taken over the 20 s interlayer waiting time. (b) Still frames of a representative layer cooling down over the 20 s interlayer waiting time.

From these plots, it can be seen that the successive layers seem to be cooling at a consistent rate over the 20 s interlayer waiting period. As expected, the temperature at $t =$

0 s decreases with each successive layer as the printed material moves away from the influence of the heated build plate. Theoretically, the material should be at 210 °C immediately after being deposited. The material cooled to approximately 130 °C in the time frame that it takes the nozzle to reach the stall position. When considering the temperature reduction seen in Figure 4.4, it should be noted that $t = 0$ s does not represent the cooling of the material as soon as it is deposited. However, it represents the time when the nozzle reaches the stalling position for the interlayer wait time described above. Capturing the temperature of the material as it is deposited would be optimal; however, this would be extremely difficult to accurately capture, due to the printing nozzle being in the field of view.

Once the nozzle reached the stall position, the material continued to cool, falling below 100 °C during the 20 s interlayer wait time before the nozzle returned to print the next layer. Figure 4.4(a) shows that there is considerable cooling over the time scales of the wait times being considered. As discussed previously, the process of the plastic material adhering to itself is thermally driven, implying that the material would not adhere to itself as well if the previous layer had cooled significantly. Similar trends can be seen between the decrease in the strength and the decrease in the temperature as interlayer wait time is increased, as shown in Figure 4.3(b) and Figure 4.4 respectively.

Another observation is that the trend of the ultimate strength of the SC samples was not as gradual as the trend seen in the TC data. The data for the 0 s wait time is noticeably higher in yield strength than all of the nonzero wait times (with a 23% decrease between the 0 s data and the 5 s data alone). A probable explanation for this lies not necessarily in the layer cooling as described with the TC specimens, but rather with printing defects caused by the wait times. Figure 4.5 compares the samples produced with different wait times. As it can be seen, the increased wait times caused poor quality of the produced shear section, which is not present in the 0 s specimen.

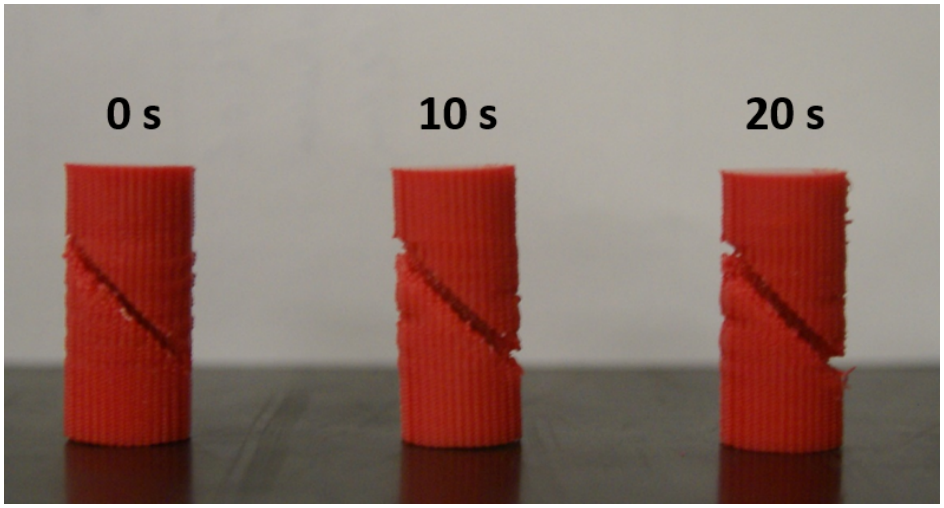

Figure 4.5. Comparison of the defects in the SC specimens caused by increasing interlayer wait time.

Although this finding sheds more light on a reduction in print quality rather than a reduction in the adhesion of successive layers due to additional interlayer cooling, it remains an important finding. Since these parts were all produced using identical printing parameters other than the interlayer wait time, they indicate that defects such as this can be the result of wait times in between printing consecutive layers of similar features. Therefore, care must be taken when considering printer retraction settings and other parameters to ensure that if a part requires such interlayer wait times for a certain part feature, they do not negatively affect mechanical properties in a significant way.

4.4 Conclusions

This chapter investigates the effects of cooling between successive layers of a sample additively manufactured out of acrylonitrile butadiene styrene (ABS) using a commercially available fused filament fabrication (FFF) machine. The results from this study showed that the cooling that happens in between successively deposited layers significantly affects the compressive and shear strength of FFF components, with approximately a 12% and 25% decrease respectively over the wait times considered (0 s to 20 s). The most significant

decrease, particularly in the shear strength, was noticed between the 0 s wait time and the 5 s wait time samples. This indicates that unless the feature sizes are sufficiently small, there will inherently be a reduction in the strength of FFF parts, purely due to the cooling in between layers.

This wait time in between the deposition of successive layers of an FFF feature is inevitable in any part beyond the most basic of geometries. These findings suggest that this wait time may have significant effects on the resulting part's strength due to the weakened interlayer bonds and defects produced. To reduce these effects, the cooling of already deposited layers must be decelerated, either using heated enclosures or other ambient heat sources, such as heat lamps. However, while these printer features may help reduce the effects of interlayer cooling, they cannot achieve the temperatures necessary to mitigate the reduction in strength all together. Additionally, certain FFF polymers will lose form during printing if they are exposed to the level of heating required to mitigate these effects. Therefore, when designing energetic structural elements out of Al/PVDF, this reduction in strength should be taken into account, especially when using a 3D printer that does not have features such as a heated build chamber.

5. THE INCORPORATION OF ATMOSPHERIC PLASMA TREATMENT WITH FUSED FILAMENT FABRICATION FOR ENHANCED POLYMER HEALING

5.1 Introduction

The work presented in this chapter seeks to build upon the work in Chapter 4 in order to enhance the mechanical properties of additively manufactured structures. While the previous chapter provided insights into which process parameters can reduce the strength of FFF components, significant progress needs to be made if the mechanical properties are going to be considered viable for structural applications. Figure 5.1 shows a plot of tensile strength results published in literature over the past twenty years as reported in a recent review paper by Peterson [57].[1]

[1]Reprinted from, Additive Manufacturing, 27, Amy M. Peterson, "Review of Acrylonitrile Butadiene Styrene in Fused Filament Fabrication: A Plastics Engineering-Focused Perspective", 363 - 371, 2019, with permission from Elsevier.

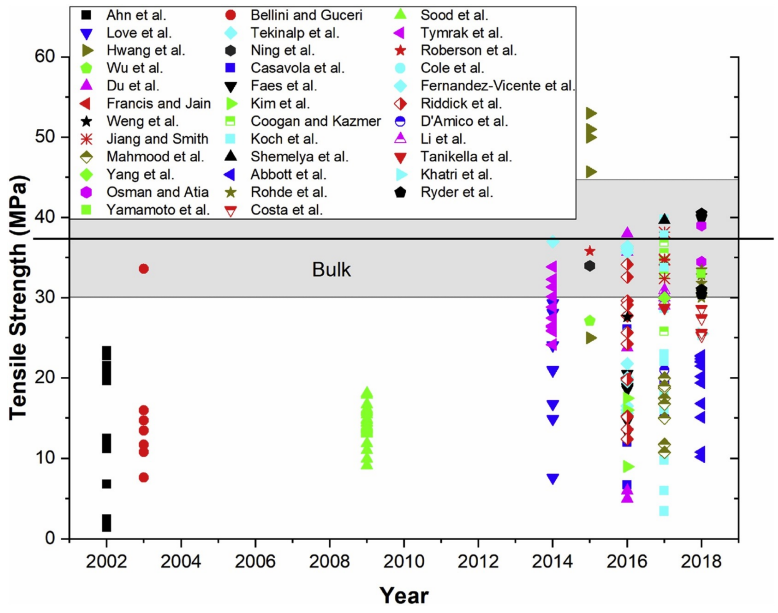

Figure 5.1. ABS tensile strength values that have been reported in literature over the past 20 years as reported by Peterson [57][1].

As can be seen, the mechanical properties are generally inferior to the bulk properties of the material, and the repeatability of the mechanical properties has not been improving in recent years. As discussed in the introduction of this document, as AM progresses towards producing end-use components, the functional properties need to be predictable and sufficient for the application. In order for this to be achieved, the phenomena causing the reduced interlayer continuity seen in AM components needs to be further investigated and the mechanical properties of additively manufactured structures need to be improved. The work in this chapter seeks to further both of these areas, by investigating the discontinuity at layer interfaces and incorporating plasma surface treatment in an attempt to improve the mechanical properties.

While there are many ongoing efforts to increase the mechanical properties of FFF components, it is important to consider the internal structure of these FFF components at the microscale in order to put these efforts into context. Figure 5.2 below shows the typical cross section of an additively manufactured component, in which porosity is naturally introduced as the material bead fails to spread into its prescribed volume as it is being deposited.

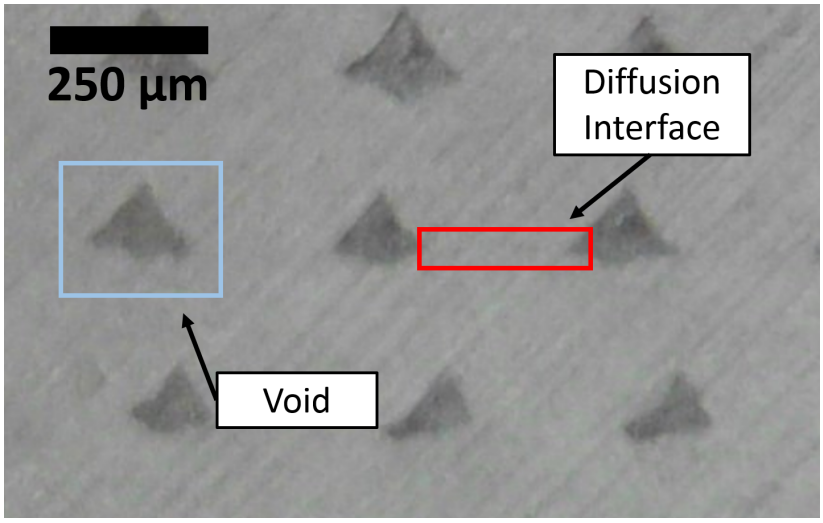

Figure 5.2. Cross section of an additively manufactured component printed using fused filament fabrication.

Two of the main aspects of the microstructure of AM components, as highlighted in Figure 5.2, that reduce the mechanical properties are the lack of material continuity at the layer interface, as well as the reduced cross-sectional area at the layer interface due to the introduced porosity [58–60]. When considering FFF applications, the lack of material continuity, highlighted by the red box in Figure 5.2, is typically driven by incomplete polymer healing when the layers are fused together [61–63]. The issue of decreased surface area contact in between the layers due to porosity, highlighted in blue, is a result of many factors in the FFF process, such as premature cooling of the polymer melt and the reduced wettability and spreading seen in polymer substrates [58, 64, 65]. The following paragraphs look at each issue respectively and discuss ongoing efforts to address the reduced mechanical properties seen in FFF components.

Polymer healing at the layer interface in FFF applications is a temperature driven process that has been well studied over the years [57, 66–70]. While Section 5.2 goes into greater detail on polymer reptation and healing, as well as accompanying modeling efforts, the strength of a polymer interface generally trends back to the polymer's bulk properties for the duration of time that the interface is held above the glass transition temperature of

the polymer, with a $t^{1/4}$ relationship. Ongoing efforts that seek to address the issue of incomplete polymer healing do so by either decreasing the effective time needed for the polymer to be completely healed or lengthening the time at which the interface remains above the glass transition temperature. Many articles have documented parametric studies that vary process parameters that modify the thermal history of the component and report the resultant mechanical properties [57,67,68,71]. Of the notable effects that seek to lengthen the time the layer interface stays above the glass transition temperature, Deshpande et al. lengthened the time by utilizing lasers to achieve pre-deposition heating [72]. Additionally, Sweeney et al. incorporated carbon nanotube (CNT) coatings on filaments, to create a shell of CNTs in between individually printed beads. Localized heating at the bead interfaces can then be achieved using microwaves, which allows for increased polymer healing [73]. One of the primary efforts that seeks to shorten the time needed for complete healing incorporates the use of ultrasonic vibration at the nozzle tip to dis-align polymer chains, priming them for reptation [74].

In terms of porosity in FFF components, the vacancies left in between adjacently printed beads, as shown in the blue region of Figure 5.2, are a result of the polymer's inability to spread effectively into it's prescribed volume before cooling. Many efforts have sought to overcome this by increasing the chamber and/or nozzle temperatures, allowing the polymer to more effectively spread [57]. However, this method can lead to a severe drop off in dimensional accuracy [66]. Other common techniques involve "overfilling" by using an extrusion multiplier, however, this too reduces dimensional accuracy [66].

This chapter seeks to improve the mechanical properties of FFF components by incorporating plasma surface treatment capabilities. Plasma treatment utilizes charged ions, created in the presence of an electric potential difference, to modify the surface chemistry of a material for enhanced adhesion and bonding [75]. It has been used in a variety of industrial applications, from increasing paint adhesion to enhancing adhesion in vapor deposition processes [75–77]. While the effects of plasma treatment are very application dependent, in theory, many of the surface modification mechanisms seen in previous uses could prove beneficial if paired with FFF processes [76]. Dowling et al. used plasma capabilities to pretreat FFF pellets and filament in order to increase the mechanical properties of AM

components [78,79]. Shih et al. introduced plasma treatment to the printing process, by dismounting the printing substrate, applying plasma treatment, and remounting the substrate to finish the printing process. The shear strength of this treated interface was then tested using quasistatic mechanical testing, which showed a significant increase in the shear strength of the interlayer bond [80]. While these efforts contribute significantly to the understanding of how plasma can effect the mechanical properties of FFF components, efforts still need to be made to incorporate plasma treatment in with the printing process, as opposed to using it as an off-printer processing technique.

The efforts in this chapter seek to address two open research questions: First, can plasma surface treatment capabilities be mounted on-board an FFF printer in order to improve the mechanical properties of the resultant printed components? And second, if improved, which aspect of the microstructure from Figure 5.2 is the plasma surface treatment improving? In order to investigate this, a traditional FFF printer was modified by mounting various plasma surface treaters on-board in various configurations. Mechanical testing was performed on the printed components in order to see how the plasma treatment affected the mechanical properties. In order to investigate how the plasma treatment affected the material continuity at the layer interface, the thermal history of the plasma treated components was compared with their untreated counterparts. In order to investigate how the plasma treatment was affecting the polymer spread and porosity, water contact angle measurements, CT scans, and wettability/spreading tests were completed.

5.2 Background and Approach

Plasma surface treatment has been used as a means to achieve better adhesion through a variety of surface modification mechanisms. In the context of FFF, these mechanisms include: (1) ablation, which refers to the breaking of the polymer's bonds when the plasma particles bombard the surface; (2) cross-linking, which refers to molecules covalently bonding with a chain on the adjacent polymer surface; and (3) surface activation, which increases the wettability of the surface by introducing functional groups into the surface chemistry [76]. In terms of the FFF process, ablation could reduce the effective polymer chain length, which

would in turn affect the diffusion scale at the layer interfaces. Additionally, within the ablation mechanism, if the energy of the plasma particles were not able to damage the bonds in the polymer, collision with the surface could cause heating of the FFF interface, which would also affect the resultant diffusion. While cross-linking is possible in the context of FFF, non-atmospheric gases would need to be present during the surface treatment process. And finally, surface activation could affect the wettability of the FFF interfaces, allowing for the polymer to more easily spread into the voids seen in Figure 5.2. This section reviews the most recent mechanical strength modeling efforts in additive manufacturing, which incorporate both of the previously discussed aspects that lead to inferior properties. While most of these modeling efforts assume idealized printing conditions, which are not practical in the context of the tests laid out in this chapter, these models provide a reliable framework for which to investigate how the plasma surface treatment is affecting the polymer healing process.

Polymer healing has traditionally been viewed as a five-step process involving surface rearrangement, surface approach, wetting, diffusion, and randomization [59,81]. Most of the healing models in the context of FFF have only accounted for the third step in the process, diffusion [61,63]. These models give insight into how the strength of FFF interfaces evolve over time, due to the diffusion (or reptation) that occurs when the interfacial temperature remains above the glass transition temperature. One of the most recent and complete mechanical strength models was introduced by Coogan et al. which considers both the wetting and diffusion aspects of the polymer healing process as a means to model both the porosity and discontinuity issues that cause the reduced mechanical properties [59]. A starting point for the strength of FFF interfaces was identified as:

$$\sigma = \sigma_0 + \sigma_D, \tag{5.1}$$

where σ is the overall strength of the interface, σ_0 is the initial strength across the interface due to wetting, and σ_D is the strength developed due to diffusion. In order to account for incomplete wetting, a wetting distribution function $\phi(t)$ was incorporated, which is a time varying fraction that accounts for the amount of the surface that is wetted. This function can account for any delay in the diffusion process due to non-instantaneous wetting, as well as effectively limit the amount of healing that can occur due to incomplete wetting. A diffusion

initiation function $\psi(t)$ was also incorporated to allow for delays in the diffusion process. Incorporating these two function results in:

$$\sigma = [\sigma_0 + \psi(t) \cdot \sigma_D] \cdot \phi(t) \tag{5.2}$$

.

When considering the diffusion strength component, σ_D, a general constant K was used, which is dependent on temperature, pressure, molecular weight, and density. Additionally, a $t^{1/4}$ term was used, which was derived from reptation theory. Reptation theory is based on individual polymer chains of length L, escaping their original prescribed location in the amorphous bulk, and moving a distance χ across the polymer-polymer interface. This was defined by:

$$\frac{\sigma_D}{\sigma_\infty} = \left(\frac{\chi}{\chi_\infty}\right) = \left(\frac{l}{L}\right)^{1/2} \tag{5.3}$$

where the normalized recovered strength, as compared to bulk strength, approaches unity when the polymer chain has moved a distance χ across the interface. χ is related via a square root to lL^{-1}, the proportion of the original chain that has moved, due to random walk. Under isothermal conditions above the glass transition temperature, the proportional chain length movement, lL^{-1}, is related via square root to tt_R^{-1}, resulting in:

$$\frac{\sigma_D}{\sigma_\infty} = \left(\frac{t}{t_R}\right)^{1/4} \tag{5.4}$$

.

Substituting this into Equation 5.2, and normalizing by the bulk strength of the material, σ_∞, the following expression is obtained:

$$\frac{\sigma}{\sigma_\infty} = [\frac{\sigma_0}{\sigma_\infty} + \underbrace{\psi(t) \cdot K \cdot (\frac{t}{t_R})^{1/4}}_{\text{Interfacial Diffusion Term}}] \cdot \underbrace{\phi(t)}_{\text{Surface Wetting Term}} \tag{5.5}$$

where t_R is the reptation time, or the time needed for the interface to heal under isothermal conditions. Coogan et al. go on to solve Equation 5.5 for an idealized printing situation, in which assumptions, empirical data, and one-dimensional thermal analysis are used to approximate a solution for the interlayer strength of their components [59]. Unfortunately, the plasma surface treatment conditions invalidate many of the assumptions needed to solve

Equation 5.5 explicitly. However, the equation can still provide a framework for how to approach the research questions previously delineated. The tests outlined in this chapter sought to isolate certain terms in this equation and investigate how the plasma treatment was affecting those terms. The first set of tests investigated the "Interfacial Diffusion Term" by analyzing the thermal history of the layer interfaces, as the diffusion kinetics at those interfaces are typically thermally driven. The second set of tests investigated the "Surface Wetting Term" by analyzing the surface water contact angle, polymer spreading, and resultant porosity, which give direct insights into how the wettability of the polymer surface is being manipulated. Section 5.3 of this chapter details how these tests were performed, and Section 5.4 shows how the plasma treatment was affecting the polymer healing process at the layer interfaces of these FFF samples and discusses the likely surface modification mechanisms that were driving the polymer healing.

5.3 Materials and Methods

5.3.1 Printer Design

In order to complete the experimentation in this chapter, a Tron XY 3D printer (Shenzhen Tronxy Technology) was modified to hold an atmospheric plasma system. While all of the experimentation was completed using a Plasma Wand system from Plasma Etch Inc., it should be noted that a Corona SB plasma system from Black Hole Labs was also investigated; however, no configuration or treatment level showed any mechanical property enhancement. In terms of mounting the plasma systems to the 3D printing gantry, two configurations were found to be successful with the Plasma Wand system. The two configurations are referred to herein as "side-by-side" and "in situ" and can be seen in Figures 5.3(a) and 5.3(b) respectively.

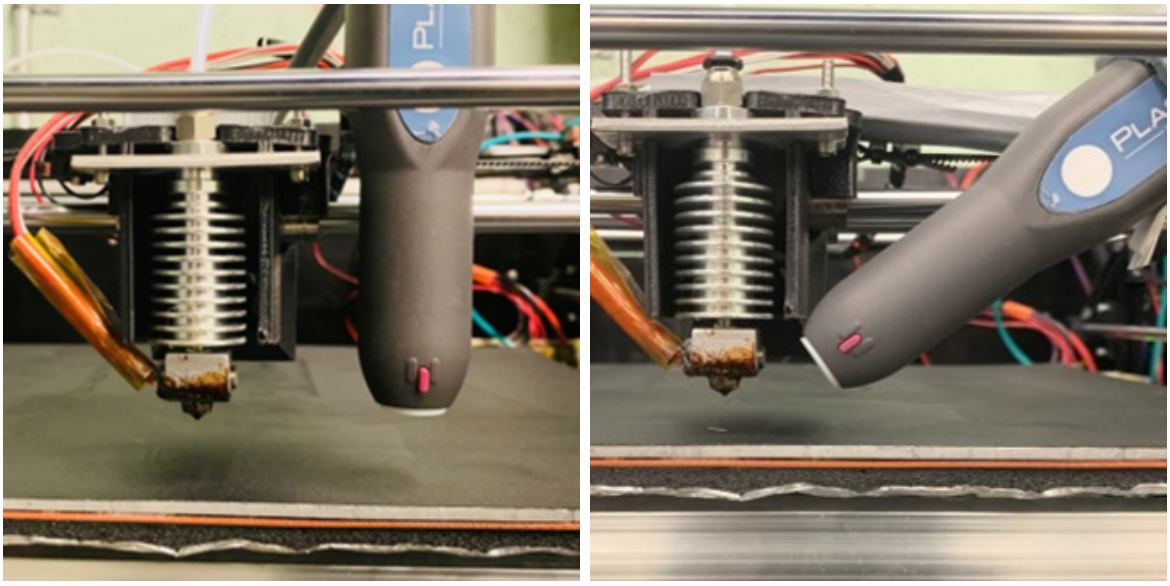

(a) (b)

Figure 5.3. (a) Side-by-side configuration of the Plasma Wand plasma treatment system. (b) In situ configuration of the Plasma Wand plasma treatment system.

The side-by-side configuration involves the plasma treatment system being aligned perpendicular to the print plane, in which a layer would be printed and then the plasma treater would be positioned over the print for a specified amount of time before the subsequent layer would be printed. For the in situ configuration, the plasma treater was oriented at a 30° orientation from the print plane, aiming directly at the point where ABS was being deposited. The configurations were shown to have a different effect on the resultant prints, as discussed later in this chapter.

It should be noted that these configurations were not optimized based on the resultant mechanical property enhancement. Ideally, further parametric studies could give insights into optimal configuration alignment, as well as the resultant modification's dependency on distance between the plasma treater and the treatment surface. Also, given the angled configuration of the in situ design, inherent directional dependencies of the treatment could expound the deviations seen in the following results. While there are limitations to the relatively simple designs used in this work, the following results gave insights into which

surface modification mechanisms were manipulating the mechanical properties, which was the ultimate goal of this work.

In addition to mounting the plasma treatment system, other modifications were made to the printer, such as adding plastic sheet walls to close off the print area. Also, a thermal IR window (FLIR, IRW-3C/3S 3 Window) was added to the front door of the printer, allowing for the monitoring of the interfacial temperature during the print. The final significant modification made to the printer included adding several electrical grounds in order to prevent damage to the printer when the plasma system would arc to the build plate.

5.3.2 Mechanical Testing

In order to investigate how the plasma surface treatment systems described in Section 5.3.1 can affect the mechanical properties of 3D printed components, shear compression samples, similar to the ones shown in Figure 4.1(a) were printed using ABS filament (Verbatim, ABS, Transparent), with the pertinent settings shown in Table 5.1. Upon initial experimentation, it was found that the 1.25 mm slot height was insufficient to allow the two halves to shear past one another without significant contact. In order to avoid the resultant friction that would complicate the mechanical property measurements, the slot height was adjusted to 5.00 mm for all of the quasi-static mechanical testing in Chapter 5. Samples were printed at various nozzle temperatures, ranging from 230 °C to 260 °C in increments of 10 °C in order to investigate the temperature dependency of any modification of the mechanical properties. 10 samples were printed at each nozzle temperature, both with and without plasma treatment, resulting in 80 samples for each of the plasma configurations. Once printed, the shear compression samples were tested in the same manner described in Section 4.2, wherein a Mark-10 compression tester was used in accordance with ASTM D695-15 [56] to obtain a stress versus strain curve, and therefore estimate the modulus of elasticity, yield strength, and maximum strength of the shear compression samples. Figure 5.5(a) in the following section shows the progression of a representative compression test, and Figure 5.5(b) details the points on the stress versus strain curve that represent the key mechanical properties that were monitored.

Table 5.1.
The important printing parameters.

Parameter	Value	Unit
Nozzle Diameter	0.4	mm
Extrusion Width	0.4	mm
Extrusion Multiplier	1.00	N/A
Layer Height	0.3	mm
Shells	0	N/A
Fill Percentage	99	%
Extrusion Temperature	230 - 260	°C
Bed Temperature	80	°C
Printing Speed	80	mm/s

5.3.3 Thermal Data Collection

The thermal response of the layer interfaces of the shear compression samples was recorded in order to compare the thermal history of the printed components. Temperature measurements were taken using a high-resolution infrared radiation (IR) camera (FLIR, A6507), using an emissivity value of 0.97. In order to preserve chamber temperature, a thermal IR window (FLIR, IRW-3C/3S 3 Window) was installed on the door of the printer as detailed in Section 5.3.1. Samples were imaged from a side-view configuration through the thermal IR window, and the temperature data reported in this chapter corresponds to layer interfaces in the slotted region of the shear compression samples, as shown in Figure 5.4.

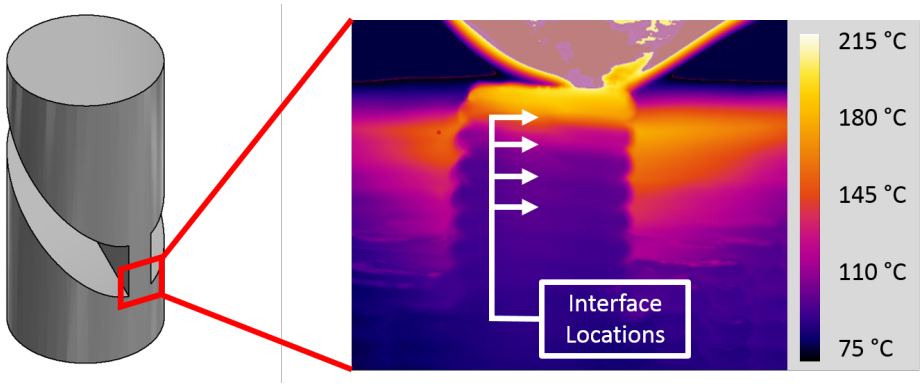

Figure 5.4. Representative thermal image displaying the location of the measurements on the Shear Compression samples.

5.3.4 Computed Tomography (CT) Scanning

Computed Tomography (CT) scans were taken of cubic samples (12 mm x 12 mm x 12 mm), which were printed with the settings shown in Table 5.1, with the exception of only using a nozzle temperature of 240 °C. Scans were taken using a Skyscan 1272 X-Ray MicroCT (Bruker) with the pertinent settings displayed in Table 5.2. The images from the CT scan were reconstructed using InstaRecon software. The porosity analysis was performed using CTAN 3D analysis software, in which the component was despeckled (<2 voxels) and shrink wrapped (radius = 2 voxels).

Table 5.2.
The CT scanning parameters.

Parameter	Value	Unit
Resolution	10	μm
Filter Materials	Al	N/A
Filter Thickness	0.25	mm
Voltage	40	kV
Current	166	μA
Rotation Step	0.2	$^\circ$
360° Scanning	No	N/A
Random Pixel Movement	No	N/A

5.3.5 Water Contact Angle Measurements

In order to investigate how the plasma treatment was affecting the surface adhesion of the ABS polymer, water contact angle measurements were performed using a drop shape analyzer (Kruss, DSA100). Substrates were prepared by printing ABS blocks (4 mm x 20 mm x 20 mm) and using a hotplate (Thermo Scientific, 200°C) to reflow the surface of the material in order to obtain a smooth measurement surface. The samples designated to receive surface modification were treated for 30 s, a time considered similar to the plasma treatment experienced by the samples discussed in Section 5.3.2. Deionized (DI) water was then pipetted in droplet sizes of 3 μL (Cole Parmer, 0.1-10 μL). The measurements, reported in Section 5.4.3, were taken using the Kruss ADVANCE software, using the sessile drop function. Five measurements were taken at each time interval shown in Figure 5.10(a).

5.3.6 Polymer Spreading Analysis

While water contact angle measurements are a standard measure of surface energy and are common when considering plasma treatment applications [75, 76, 78, 80, 82], polymer

spreading tests, as seen in [59], were performed to quantify the amount of spreading seen in the polymer. The purpose of these measurements was to directly measure how the plasma treatment was affecting the wettability of the ABS surface in a more realistic printing scenario that simulates the plasma treatment-deposition process seen when preparing the shear compression samples. The samples printed, hereafter referred to as wettability samples, consisted of 4 single bead width walls, printed in a rectangular pattern (7 mm x 19 mm) with a sample height of 9 mm. The wettability samples were printed with the same settings as shown in Table 5.1, with the exception of a slower print speed (10 mm/s), which was reduced to simulate a similar plasma treatment time as the shear compression samples. Both the side-by-side treatment method, and the in situ treatment method, were considered for this analysis.

Once printed, the wettability samples were placed in a 3D printed, rectangular prism mold (Internal Dimensions: 9 mm x 25 mm x 10 mm), and cast in a two part epoxy (Art N' Glow, clear epoxy resin) tinted with black acrylic. Once set, the samples were able to sectioned using a low-speed sectioning saw (IsoMet LS, 30 HC Blade) in order to reduce the damage to the cross-sectional face. The printed beads were then measured for the bead width, as well as the bond width, to obtain the $f_{wetting}$ term seen in [59]:

$$f_{wetting} = \frac{bond\,width}{bead\,width}. \tag{5.6}$$

This term can be used as a measure of how the printed bead is spreading onto the previously deposited layer, and therefore determine how the plasma treatment is affecting polymer wetting and spreading process during the print.

5.4 Results and Discussion

5.4.1 Mechanical Analysis and Corresponding Potential Plasma Treatment Mechanisms

In order to answer the first research question, which seeks to improve the mechanical properties of FFF components using on-board plasma treatment, the shear compression

samples described in Section 5.3.2 were quasistatically tested in order to obtain the modulus of elasticity, the yield strength, and the ultimate strength of the samples. Figure 5.5(a) shows the progression of a representative compression test, and Figure 5.5(b) details the points on the stress versus strain curve that represent the key mechanical properties that were monitored.

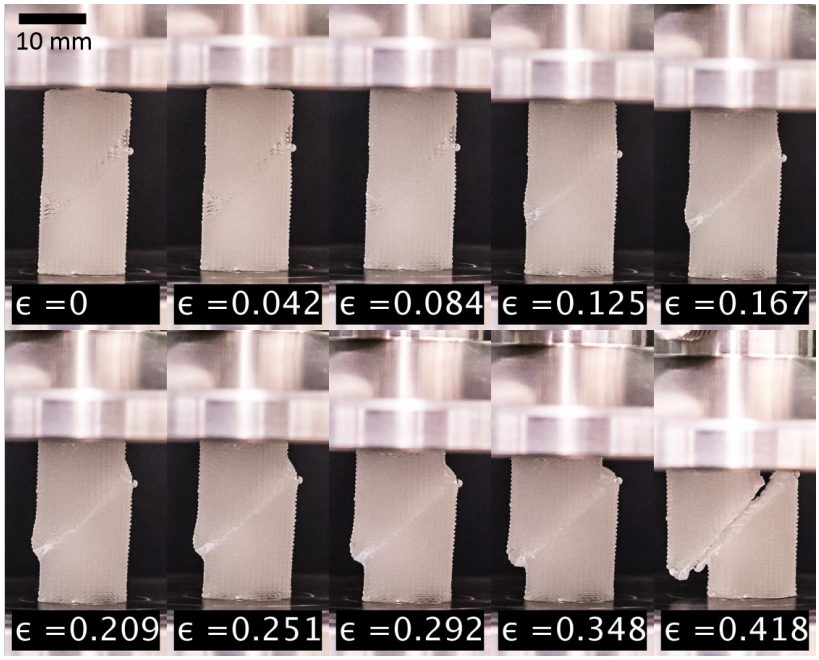

(a)

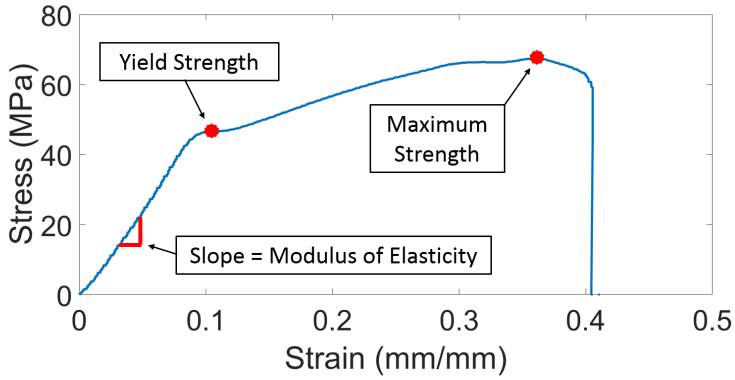

(b)

Figure 5.5. (a) Progression of a compression test of a representative shear compression sample. (b) Resultant stress versus strain curve that identifies the key properties that were monitored during the mechanical property analysis.

The mechanical properties shown in Figure 5.5(b) were recorded for all 160 shear compression samples. Plots of the mechanical properties can be seen as a function of nozzle temperature in Figure 5.6 for the side-by-side configuration and in Figure 5.7 for the in situ configuration. Each point on a plot represents the average of the 10 samples for that sample's printing condition, with the error bounds representing 1 standard deviation. The samples printed with plasma treatment are shown in purple, where as baseline samples without plasma treatment are shown in black.

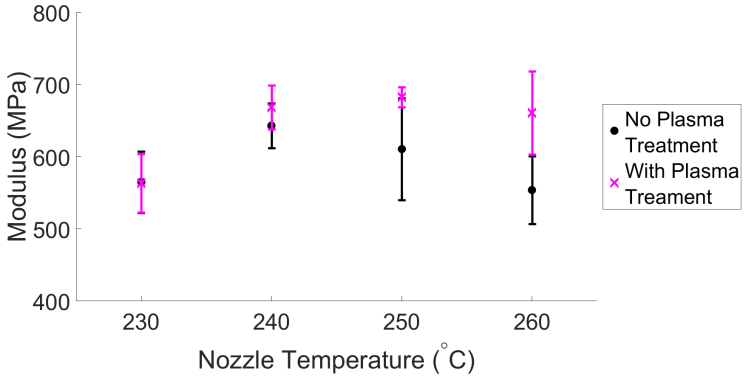

(a)

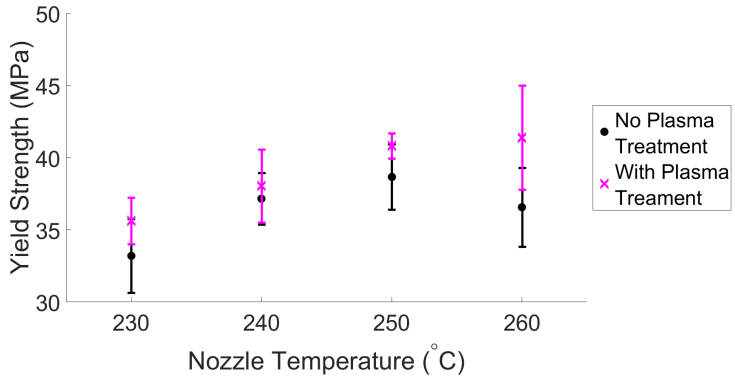

(b)

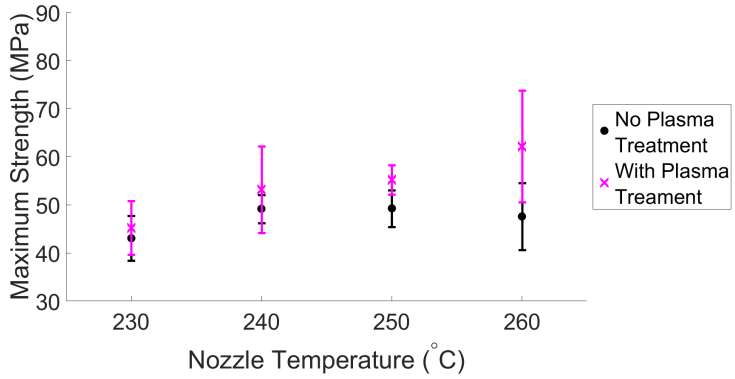

(c)

Figure 5.6. (a) Modulus of elasticity plotted versus nozzle temperature for the side-by-side configuration. (b) Yield stress plotted versus nozzle temperature for the side-by-side configuration. (c) Maximum stress plotted versus nozzle temperature for the side-by-side configuration.

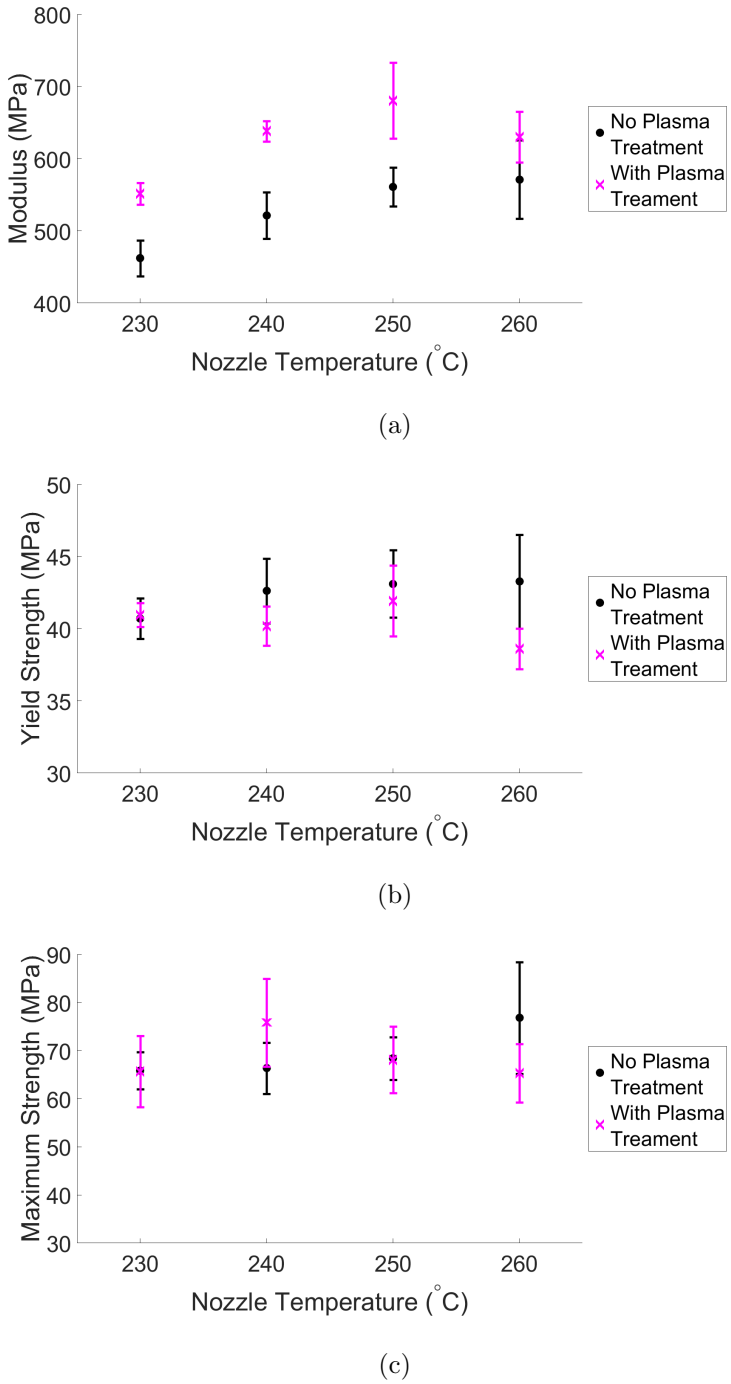

Figure 5.7. (a) Modulus of elasticity plotted versus nozzle temperature for the in situ configuration. (b) Yield stress plotted versus nozzle temperature for the in situ configuration. (c) Maximum stress plotted versus nozzle temperature for the in situ configuration.

From Figures 5.6 and 5.7, it can be seen that the plasma surface treatment was affecting the mechanical properties for both of the plasma mounting configurations. The most significant increase was seen in the modulus of elasticity of the samples printed using the in situ configuration, which saw an average increase of 18% across all of the nozzle temperatures. While the in situ treatment configuration significantly increased the modulus of elasticity, the other mechanical properties that were considered, the yield strength and the maximum strength, saw more ambiguous results and a significant increase in strength was not seen. The side-by-side configuration saw more consistent increases in mechanical properties, though less significant. For the side-by-side configuration, the plasma treatment increased the modulus of elasticity, the yield strength, and the maximum strength for every nozzle temperature that was used. While the increase was consistent, the error seen in these scenarios makes the increases less notable, though still present. It should be noted there was considerable variation in the mechanical property measurements, as well as many of the other measurements recorded in this chapter. This was attributed to the variable nature of the FFF process, which has historically shown similar deviations [57].

While most of the scenarios shown in Figures 5.6 and 5.7 answer the first research question of this chapter, demonstrating the ability to increase the mechanical properties of FFF components using on-board FFF treatment, the mechanical analysis alone does not provide sufficient information to answer the second research question, which seeks to identify the underlying plasma surface modification mechanism that was driving the improvement of mechanical properties. If considering the plasma treatment as a process parameter, the mechanical properties previously discussed show how this parameter affects the structural properties of these FFF components. However, when attempting to identify how the plasma treatment was affecting the entire polymer healing process, as modeled by Equation 5.5, the individual aspects of the polymer healing process need to be considered. To reiterate the mechanisms likely to result in increased adhesion in FFF processes, this study considers the effects of the plasma on the diffusion at the layer interface due to ablation, as well increased wettability due to the functional groups introduced during surface activation. As covalent bonding is typically seen when using higher power plasma treatment systems, as well as non-atmospheric gases, it was not considered in this study. The rest of the experiments seek

to isolate the wettability and diffusion aspects of the polymer healing process in order to determine how they are contributing to the interlayer strengths shown in Figures 5.6 and 5.7.

5.4.2 Analysis of Polymer Diffusion

The diffusion kinetics at the layer interfaces are typically dictated by the thermal history of those interfaces [57, 59]. The normalized bond strength due to these diffusion kinetics approaches unity as t approaches t_R, a finite time required for the interface to be above the glass transition temperature of the polymer. While the constants in Equation 5.5 only hold for isothermal conditions, which is not applicable in FFF, the time that the interface is held above the glass transition temperature is a reliable metric that should give insights into the expected change in mechanical properties.

This is demonstrated in Figure 5.8(a), which shows the thermal history of a single layer of the slotted region of a shear compression sample printed using the side-by-side technique for the four nozzle temperatures considered. Using this data, the time at which the interface was kept above glass transition temperature can be calculated, which is shown in Figure 5.8(b) plotted along with the corresponding mechanical properties. The time at which the interface is held above the glass transition temperature was effectively extended by increasing the nozzle temperature, which resulted in an increase in mechanical properties.

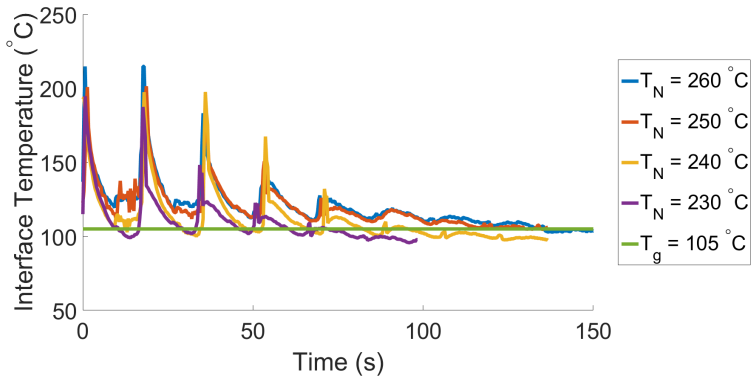

(a)

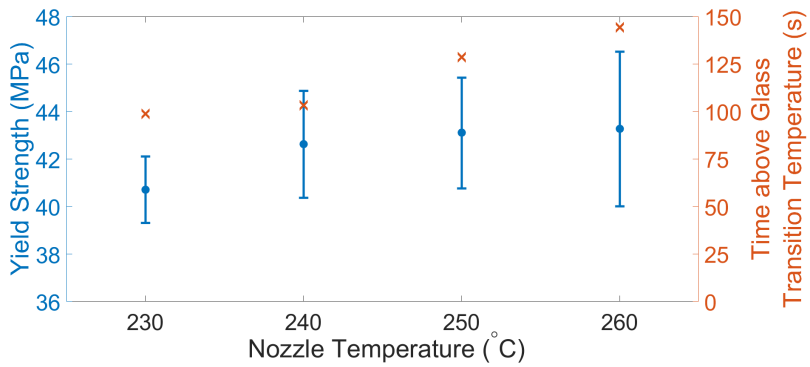

(b)

Figure 5.8. (a) The interface temperature measured as a function of time for samples printed at different nozzle temperatures. (b) The time above the glass transition temperature, as well as maximum strength, plotted versus nozzle temperature.

Given this relationship, it is important to consider how the plasma treatment was affecting the thermal history, and therefore the polymer healing process, of the shear compression components. Figure 5.9 shows the thermal history of samples printed with a nozzle temperature of 240 °C both in the side-by-side configuration [Figure 5.9(a)], as well as the in situ configuration [Figure 5.9(b)].

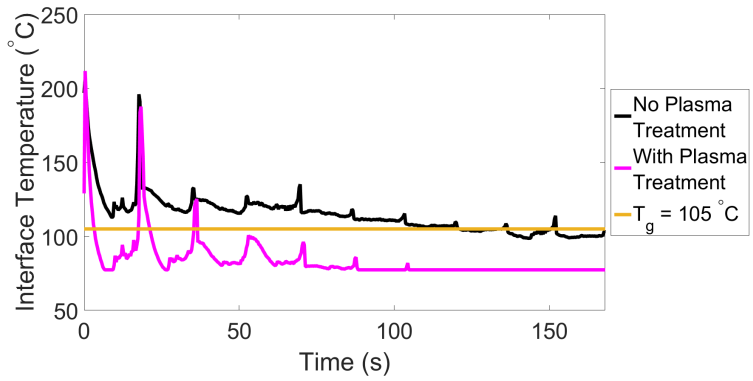

(a)

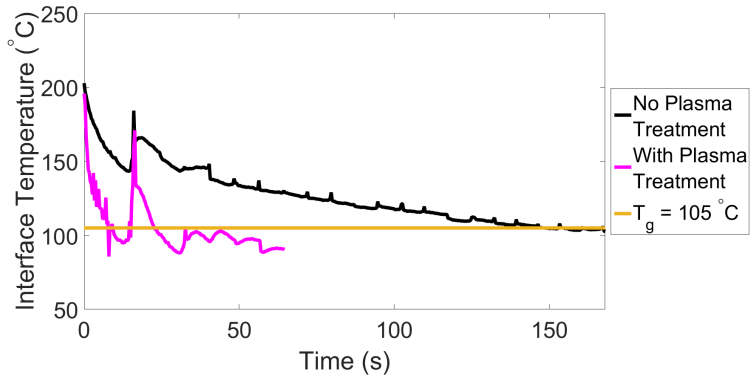

(b)

Figure 5.9. (a) The interface temperature verses time for samples printed with a nozzle temperature of 240 °C using the side-by-side configuration. (b) The interface temperature verses time for samples printed with a nozzle temperature of 240 °C using the in situ configuration.

Figure 5.9 shows that the time the interface was spending above the glass transition temperature is being shortened by the plasma treatment due to convective heat losses caused by the delivery mechanism of the plasma. Based on this alone, the strength of the component would be expected to decrease, not increase as seen in Figure 5.6. This phenomena is demonstrated well in Chapter 4, in which the strength of the shear compression samples, as well as true compression samples, were reduced through a similar thermal history modifications.

Additionally, it should be discussed that the diffusion kinetics are dependent on the polymer's chain length. Significant ablation could result in polymer scission, modifying the

resultant diffusion, and significantly reducing the reptation time needed for complete polymer healing. Based on the mechanical results seen in Figures 5.6 and 5.7, in which the general polymer healing trend is not significantly affected, polymer scission was not suspected to have a significant influence on the polymer healing process.

In summary, when considering the thermal history of the components, a shorter time above the glass transition temperature was noticed when the plasma treatment was being used. As this effect typically decreases the overall bond strength, it is suspected that another aspect of the plasma treatment is the driving mechanism of the increased mechanical properties.

5.4.3 Polymer Spreading and Wettability

The final set of experiments discussed in this chapter investigate how the plasma treatment was affecting the wettability of the polymer surface. Increased wettability is one of the most common plasma surface modification mechanisms and is a result of introduced functional groups that increase the adhesion properties of the polymer surface [76]. As polymer healing due to diffusion cannot occur until polymer wetting is complete, any modifications to this parameter can significantly affect the resultant interfacial strength. Three sets of tests, as laid out in Section 5.3, were used to investigate how the plasma was affecting the wettability of the polymer surface.

The first test, and most commonly seen in literature, looks at how the plasma treatment was affecting the water contact angle of the substrate. Figure 5.10 shows how the water contact angle on the ABS substrate was shifted by the plasma modification and evolving over time, with Figure 5.10(a) showing the average of five measurements at each time interval and Figure 5.10(b) showing representative water contact angle measurements.

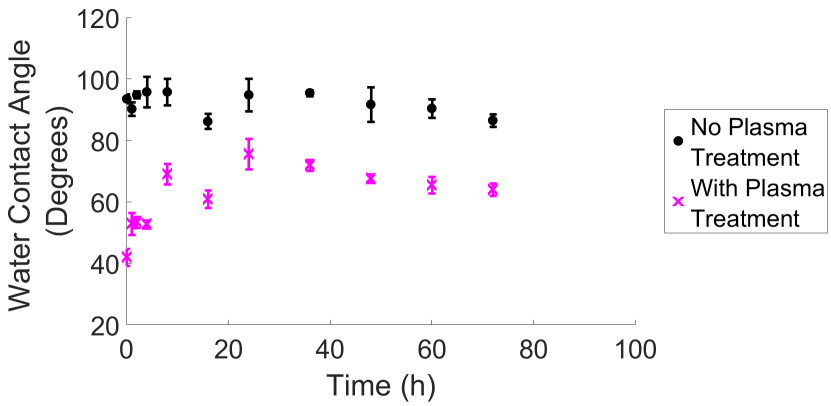

(a)

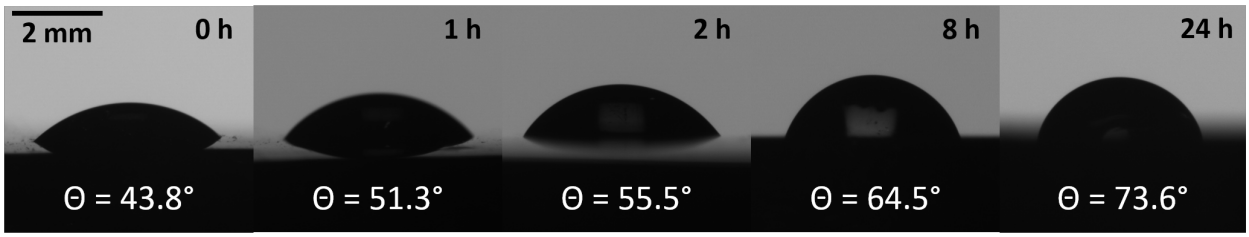

(b)

Figure 5.10. (a) Plot showing water contact angle verses time, demonstrating how the plasma treatment is affecting the surface chemistry of the polymer. (b) Representative water contact angle measurements at various time intervals.

As can be seen, the water contact angle was significantly reduced in the plasma treated substrates. For the plasma treated substrates, the contact angle was reduced to 43° and then rebounded over time. For the untreated samples, the water contact holds relatively steady around 90°, which is similar to other results seen in literature [78]. As water contact angle is inversely related to wettability, these water contact angle measurements support the theory of increased wettability resulting in an increase in mechanical properties.

The next set of tests used to examine how the plasma was modifying the wettability is by determining its effect on the wettability factor, defined in Section 5.3.6. The wettability samples previously described were printed in both the side-by-side and in situ configurations. Images of one of the sample's cross sections is shown in Figure 5.11 along with a representative

wettability factor ($f_{wetting}$) measurement. The results of the wettability factor tests are summarized in Table 5.3.

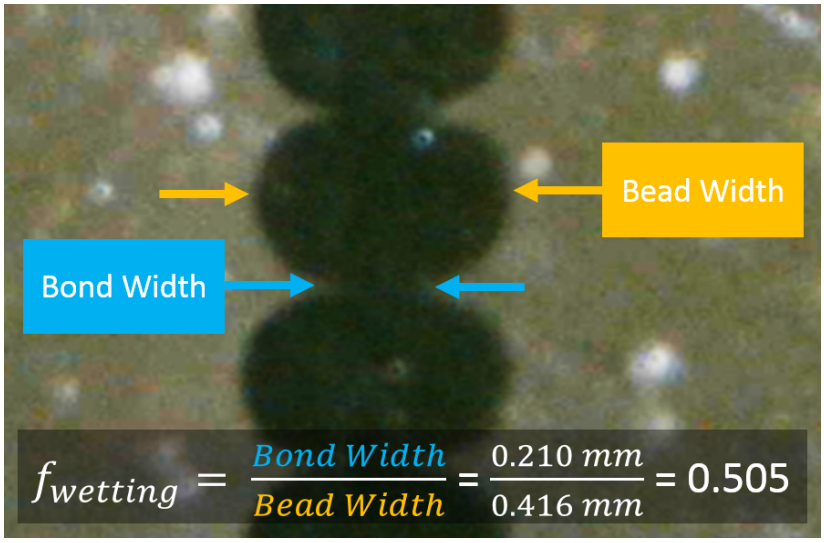

Figure 5.11. Images of a cross section of a wettability sample with a representative wettability factor measurement.

Table 5.3.
The wettability results determined by polymer spreading analysis.

	No Plasma Treatment		With Plasma Treatment	
	Side-by-Side	In Situ	Side-by-Side	In Situ
Average Bead Width (mm)	0.374	0.415	0.366	0.406
Average Bond Width (mm)	0.160	0.211	0.174	0.217
$f_{wetting}$	0.427	0.509	0.477	0.534

As can be seen, the wettability factor was increased when using the plasma surface treatment, regardless of the configuration. The wettability factor was increased by 11.7% and 4.9% for the side-by-side and in situ configurations respectively. This test also gives credence to the theory of increasing the wettability of the surface, and therefore effectively

lengthening the bondwidth in the printed samples. Also, an observation was made that the wettability factor increased when going from the side-by-side configuration to the in situ configuration. This is likely due to the increased time that the interfacial temperature remains above the glass transition temperature of the material, a trend also reported by Coogan et al. [59]. This observation makes intuitive physical sense, as the ability for the polymer to spread is correlated to the viscosity of the polymer melt, which is temperature dependent. This observation could be an explanation for the slight temperature dependence of the increase in mechanical properties seen in Figure 5.6.

The final test investigating how the plasma was affecting the wettability seeks to quantify the porosity seen in printed components. Porosity, as shown in Figure 5.2, affects the amount of surface area that is in contact from one printed bead to the next. The final porosity would be correlative to the wettability, in which a higher fraction of wetted surface area results in reduced porosity and higher strength. Three cubes were printed with and without plasma surface treatment using the in situ configuration. Figure 5.12(a) shows a representative ABS cube that was prepared for porosity analysis. Figure 5.12(b) shows the resultant CT scan of the sample shown in Figure 5.12(a). The results of the porosity analysis of the scanned cubes are summarized below in Table 5.4.

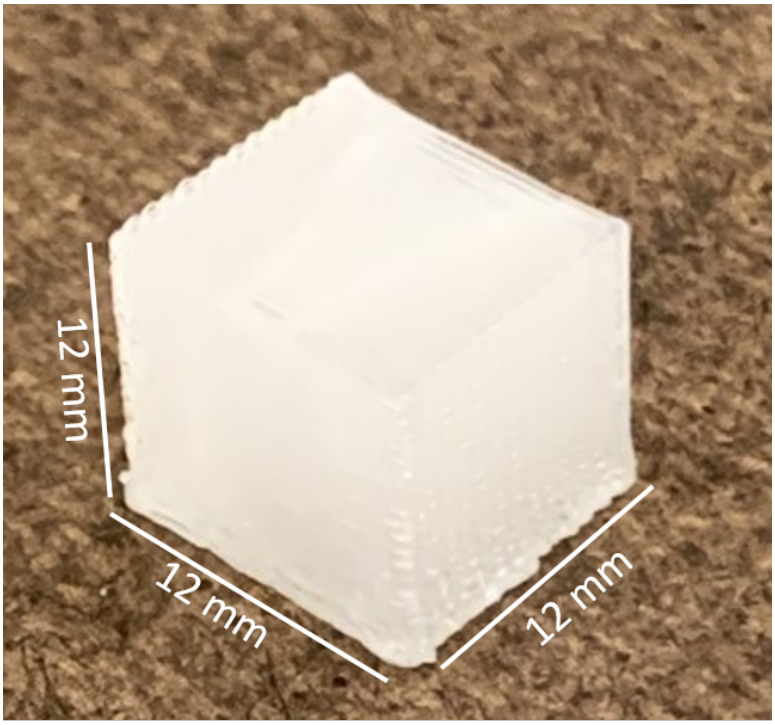

(a)

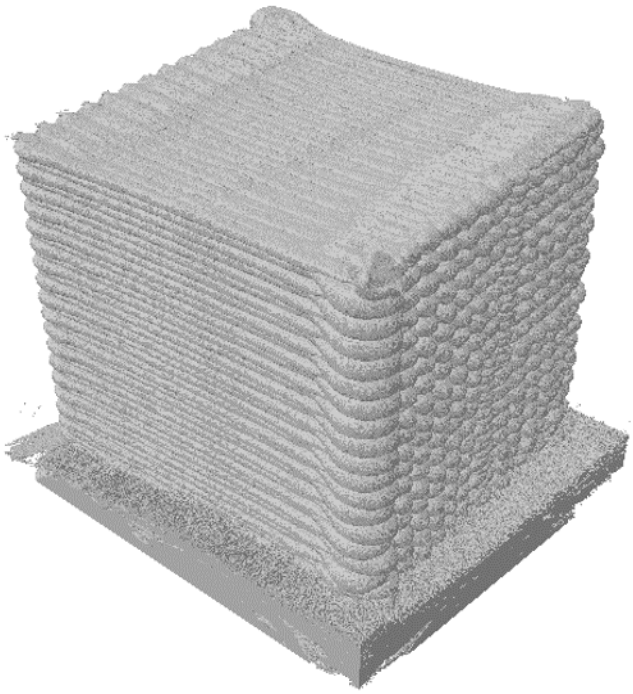

(b)

Figure 5.12. (a) Representative cubic sample used for the porosity analysis via CT scanning. (b) Resultant CT scan of sample shown in (a).

Table 5.4.
CT scanning results for all of the samples that were considered.

	No Plasma Treatment		With Plasma Treatment	
Sample Number	Closed Porosity (%)	Total Porosity (%)	Closed Porosity (%)	Total Porosity (%)
Sample 1	2.80	3.66	1.76	2.03
Sample 2	2.98	3.48	2.35	2.66
Sample 3	2.59	2.92	2.82	3.20
Average	2.79	3.35	2.31	2.63

It should be noted that the limited sample set shown in Table 5.4 is insufficient to draw significant conclusions, and outliers were noticed in the displayed results. However, initial results indicate a reduction in porosity, which once again points to increased wettability as the driving plasma treatment mechanism that is causing the increased mechanical properties.

In conclusion, the final three tests in this section (water contact angle, polymer spreading, and porosity analysis), all indicate that the polymer's surface wetting characteristics are being manipulated. It should be noted that these tests primarily give insights into the steady state value of $\phi(t)$ as shown in Equation 5.5. In order to investigate the full extent to which $\phi(t)$ is affected by the surface modification, how the wetted surface evolves over time needs to be considered. The fact that surface wetting is necessary in order for diffusion to occur, paired with the relatively short time scales at over which the interfacial temperature drops significantly below the nozzle temperature, any transient nature of the $\phi(t)$ term could have significant implications on the resultant interfacial strength.

5.5 Conclusions

From this experimentation, the ability to increase the mechanical properties of FFF components using on-board plasma treatment was demonstrated. The thermal history was analyzed and it was hypothesized that enhanced diffusion at the layer interface was not a

significant contributor, but a rather a detractor from, the improved mechanical properties in this system. A variety of tests investigating how the plasma treatment was affecting the wettability of the surface were performed and all of the tests indicated that the wettability was increased during treatment and is likely the driving mechanism causing the improvement seen in the mechanical properties. These tests give insight into how to pair plasma surface treatment with FFF systems. Future work would include continued investigation of the surface wettability, specifically looking for any transient behavior as discussed previously. Also, future experimentation should include tuning the plasma treatment process and thermal history control in order to optimize the mechanical strength of the FFF components. Additionally, other plasma treatment mechanisms, such as cross-linking, should be investigated for their viability to be incorporated into the FFF process.

6. CONCLUSIONS

6.1 Conclusions

The work in this document furthered the field of additive manufacturing by contributing to two significant areas. The first area contributed to the additive manufacturing of energetic materials by developing post-print characterization techniques and quantifying the functional abilities of 3D printed energetic materials. A significant portion of the work focused on characterizing FFF components printed using an Al/PVDF energetic material developed by Fleck et al. in a prelude to this work. The analysis of the printed Al/PVDF structures developed an understanding for the functional capabilities of this MESM. Additionally, material-process-function relationships were investigated in order to understand which key parameters of the AM process will most significantly affect the structural energetic properties of the material. This work, highlighted in Chapters 2 and 3, will now allow for the easier implementation of the Al/PVDF material as a structural energetic material.

Chapter 2 of this document focused on determining the effect of the material constituents on the structural energetic properties of the material. Seven different formulations with various particle loadings and particle sizes were examined, based on their compatibly with FFF printing. The modulus of elasticity and the ultimate strength were plotted as a function of both particle loading and particle size. The energetic capabilities of the material were predicted using thermochemical codes. These predictions were then verified with burning rate measurements and DSC/TGA analysis. This analysis allowed for visualization of how the mechanical properties and the combustion properties are related.

Once an understanding of how the material constituents affect the structural energetic properties of the Al/PVDF material was gained, how the AM process affects those same properties was examined in Chapter 3. The same post-print characterization process was used, wherein burning rate samples and ASTM Type V dogbones were 3D printed while holding the material formulation consistent. The only variation was the print direction,

which was varied between 0° and 90° orientations. Only these two orientations were chosen as extensive literature on inert materials showed these displayed the extreme mechanical properties. This analysis showed that the ultimate strength and modulus of elasticity were dependent on the print direction, both decreasing as the orientation transitioned from 0° to 90°. The burning rate, a very common energetic performance metric, was not shown to have a significant dependence on the print direction. Beyond the variation of print direction, two realistic energetic structural elements were designed. Via 3-point bending analysis, these two trusses demonstrated the ability to tune the structural energetic performance of these elements during the design phase.

The second significant area in which this work contributes to AM is through the study of the polymer healing process as it pertains to FFF applications by investigating the decreased adhesion at the layer interfaces. During the analysis of the dogbones used in the print direction study (Chapter 3), it was observed that the failure of the 90° samples occurred at the bead-to-bead interface, which prompted an investigation into the mechanical properties of FFF components using inert materials, primarily ABS. As the process of adhering one layer to another in FFF is known to be thermally driven, Chapter 4 quantified the relationship between the amount of interlayer cooling and the mechanical strength of the component (a representation of how well the layers were fusing together). The amount of cooling that is allowed before the subsequent material is fused to it is determined by a wide variety of printing parameters, such as feature size, processing temperatures, printing speeds, etc. While the amount of cooling may vary greatly for any given print, this analysis should give insight into which parameters should be closely monitored if the structural performance of the material is critical.

The fifth and final chapter of this document explored incorporating plasma surface treatment to improve the inferior mechanical properties seen in Chapters 3 and 4. The ability to increase the mechanical properties of FFF components using on-board plasma treatment capabilities was demonstrated. The thermal history was analyzed and it was hypothesized that enhanced diffusion at the layer interface was not a significant contributor, but a rather a detractor from, the improved mechanical properties in this system. A variety of tests investigating how the plasma treatment was affecting the wettability of the surface were performed

and all of the tests indicated that the wettability was increased during treatment and is likely the driving mechanism causing the improvement seen in the mechanical properties. These tests give initial insight into how to successfully pair plasma treatment with FFF printers and give insights into how that plasma treatment can affect the polymer healing process in FFF applications.

This body of work advances additive manufacturing closer to being able to manufacture functional, end-use products, which has been one of the major focuses of additive manufacturing research over past decade. The work pertaining to the additive manufacturing of energetic materials gives insights into the design of MESMs for additive applications and lays the ground work for the basic studies that should be completed in order to understand how the printing process affects the structural energetic properties of additively manufactured energetic materials. The work pertaining to the investigation of the polymer healing process gives insights into what mechanisms drive the reduced mechanical properties seen in FFF components and presents a method to help improve them. As a whole, this work contributed to the needs of the additive manufacturing of energetic materials community, as well as the additive manufacturing community as at large.

REFERENCES

[1] K.V. Wong, A. Hernandez, A Review of Additive Manufacturing, ISRN Mechanical Engineering 2012.

[2] B.N. Turner, R. Strong, S.A. Gold, A Review of Melt Extrusion Additive Manufacturing Processes: I. Process Design and Modeling, Rapid Prototyping Journal 2014, 20(3), 192-204.

[3] B.N. Turner, S.A. Gold, A Review of Melt Extrusion Additive Manufacturing Processes: II. Materials, Dimensional Accuracy, and Surface Roughness, Rapid Prototyping Journal 2015, 21(3), 250-261.

[4] Ultimaker PC, Ultimaker B.V. (2019) URL: ultimaker.com/en/products/materials/pc.

[5] Conductive Graphene PLA Filament, Black Magic 3D. (2019) URL: http://www.blackmagic3d.com/Conductive-p/grphn-pla.htm.

[6] Ultimaker CPE Family, Ultimaker B.V. (2019) URL: https://ultimaker.com/en/products/materials/cpe.

[7] O.S. Es-Said, J. Foyos, R. Noorani, Effect of Layer Orientation on Mechanical Properties of Rapid Prototyped Samples, Material Manufacturing and Processes 2000, 15(1), 107-122.

[8] S.H. Ahn, M. Montero, D. Odell, Anisotropic Material Properties of Fused Deposition Modeling ABS, Rapid Prototyping Journal 2002, 8(4), 248-257.

[9] K. Upadhyay, R. Dwivedi, A.K. Singh, Determination and Comparison of the Anisotropic Strengths of Fused Deposition Modeling, In: Advances in 3D Printing & Additive Manufacturing Technologies. Singapore, Singapore: Springer 2017, 9-28.

[10] C.S. Lee, S.G. Kim, H.J. Kim, Measurement of Anisotropic Compressive Strength of Rapid Prototyping Parts, Journal of Material Processing Technology 2007, 187, 627-630.

[11] A. Dorigato, V. Moretti, S. Dul, S.H Unterberger, A. Pegoretti, Electrically Conductive Nanocomposites for Fused Deposition Modelling, Synthetic Metals 2017, 226, 7-14.

[12] A.K. Sikder, N. Sikder, A Review of Advanced High Performance, Insensitive and Thermally Stable Energetic Materials Emerging for Military and Space Applications, Journal of Hazardous Materials 2004, 112(12), 1-15.

[13] T.J. Fleck, A.K. Murray, I.E. Gunduz, S.F. Son, G.T.-C. Chiu, J.F. Rhoads, Additive Manufacturing of Multifunctional Reactive Materials, Additive Manufacturing 2017, 17, 176-182.

[14] C. Fritz, O. Wilhelm, Solid Rocket Propellants, US Patent 3,429,264, Nitrochemie Gmbh, 1969.

[15] C. Rossi, S. Orieux, B. Larangot, T. Do Conto, D. Esteve, Design, Fabrication and Modeling of Solid Propellant Microrocket-Application to Micropropulsion, Sensors and Actuators A: Physical 2002, 99(12), 125-133.

[16] J.B. Canterberry, U.S. Patent No. 5,062,365, Washington, DC: U.S. Patent and Trademark Office 1991.

[17] S.M. Danali, R.S. Palaiah, and K.C. Raha, Developments in Pyrotechnics (Review Paper), Defense Science Journal 2010, 60(2), 152-158.

[18] F.D. Ruz-Nuglo, L.J. Groven, 3D Printing and Development of Fluoropolymer Based Reactive Inks, Advanced Engineering Materials 2018, 20(2), 1700390.

[19] A.K. Murray, W.A. Novotny, T.J. Fleck, I.E. Gunduz, S.F. Son, G.T.-C. Chiu, J.F. Rhoads, Selectively-Deposited Energetic Materials: A Feasibility Study of the Piezoelectric Inkjet Printing of Nanothermites, Additive Manufacturing 2018, 22, 69-74.

[20] C. Huang, G. Jian, J.B. DeLisio, H. Wang, M.R. Zachariah, Electrospray Deposition of Energetic Polymer Nanocomposites with High Mass Particle Loadings: A Prelude to 3D Printing of Rocket Motors, Advanced Engineering Materials 2015, 17(1), 95-101.

[21] M.J. Mezger, L.J. Groven, Printed Energetics: The Path toward Additive Manufacturing of Munitions, CRC Press, Energetic Materials 2017, 115-128.

[22] M.M Durban, A.M. Golobic, E.V. Bukovsky, A.E. Gash, K.T. Sullivan, Development and Characterization of 3D Printable Thermite Component Materials, Advanced Materials Technologies 2018, 3(12), 1800120.

[23] X. Wang, M. Jiang, Z. Zhou, J. Gou, D. Hui, 3D Printing of Polymer Matrix Composites: A Review and Prospective, Composites Part B: Engineering 2017, 110, 442-458.

[24] I.E. Gunduz, M.S. McClain, P. Cattani, G.T.C. Chiu, J.F. Rhoads, S.F. Son, 3D Printing of Extremely Viscous Materials using Ultrasonic Vibrations, Additive Manufacturing 2018, 22, 98-103.

[25] M.S. McClain, I.E. Gunduz, S.F. Son, Additive Manufacturing of Ammonium Perchlorate Composite Propellant with High Solids Loadings, Proceedings of the Combustion Institute 2018, 37(3), 3135-3142.

[26] M.H. Straathof, C.A. van Driel, J.N. van Lingen, B.L. Ingenhut, A.T. ten Cate, H.H. Maalderink, Development of Propellant Compositions for Vat Photopolymerization Additive Manufacturing, Propellants, Explosives, Pyrotechnics 2020, 45(1), 36-52.

[27] J.A. Bencomo, S.T. Iacono, J. McCollum, 3D Printing Multifunctional Fluorinated Nanocomposites: Tuning Electroactivity, Rheology and Chemical Reactivity, Journal of Materials Chemistry A 2018, 6(26), 12308-12315.

[28] R. Zaharieva, S. Hanagud, Preliminary Design of Multifunctional Structural-Energetic Materials for High Density, High Strength and Release of High Enthalpic Energy, International Journal of Scientific Engineering and Technology 2014, 3(9), 1189-1192.

[29] X.F. Zhang, A.S. Shi, L. Qiao, J. Zhang, Y.G. Zhang, Z.W. Guan, Experimental Study on Impact-Initiated Characters of Multifunctional Energetic Structural Materials, Journal of Applied Physics 2013, 113(8), 083508.

[30] M. Martin, S. Hanagud, N.N. Thadhani, Mechanical Behavior of Nickel+ Aluminum Powder-Reinforced Epoxy Composite, Materials Science and Engineering: A 2007, 443(1-2), 209-218.

[31] J.M. Chacon, M.A. Caminero, E. Garcia-Plaza, P.J. Nunez, Additive Manufacturing of PLA Structures using Fused Deposition Modelling: Effect of Process Parameters on Mechanical Properties and their Optimal Selection, Materials and Design 2017, 124, 143-157.

[32] J.F. Rodriguez, J.P. Thomas, J.E. Renaud, Mechanical Behavior of Acrylonitrile Butadiene Styrene (ABS) Fused Deposition Materials Experimental Investigation, Rapid Prototyping Journal 2001, 7(30), 148-158.

[33] J.F. Rodriguez, J.P. Thomas, J.E. Renaud, Design of Fused-Deposition ABS Components for Stiffness and Strength, Journal of Mechanical Design 2003, 125(3), 545-551.

[34] M.J. Ward, S.F. Son, M.Q. Brewster, Steady Deflagration of HMX with Simple Kinetics: A Gas Phase Chain Reaction Model, Combustion and Flame 1998, 114(3-4), 556-568.

[35] T.J. Fleck, T.D. Manship, S.F. Son, J.F. Rhoads, The Effect of Process Parameters on the Mechanical Properties of Additively Manufactured Lightweight Reactive Structures, Accepted by Journal of Engineering Materials and Technology.

[36] A.K. Sood, R.K. Ohdar, S.S. Mahapatra, Experimental Investigation and Empirical Modelling of FDM Process for Compressive Strength Improvement, Journal of Advanced Research 2012, 3(1), 81-90.

[37] R.B. Dinwiddie, V. Kunc, J.M. Lindal, Infrared Imaging of the Polymer 3D-Printing Process, Thermal Infrared Applications XXXVI 2014, 9105 (910502).

[38] K. Meeks, M.L. Pantoya, C. Apblett, Deposition and Characterization of Energetic Thin Films, Combustion and Flame 2014, 161(4), 1117-1124.

[39] S.K. Valluri, M. Schoenitz, E. Dreizin, Fluorine-Containing Oxidizers for Metal Fuels in Energetic Formulations, Defence Technology 2018, 15(1), 1-22.

[40] C.D. Yarrington, S.F. Son, T.J. Foley, Combustion of Silicon/Teflon/Viton and Aluminum/Teflon/Viton Energetic Composites, Journal of Propulsion and Power 2010, 26(4), 734-743.

[41] X. Li, M.R. Zachariah, Direct-Deposition to Create High Particle Loading Propellants with Controlled Architecture: Combustion And Mechanical Properties, In 54th AIAA Aerospace Sciences Meeting 2016, 0688.

[42] H.A. Miller, B.S. Kusel, S.T. Danielson, J.W. Neat, E.K. Avjian, S.N. Pierson, S.M. Budy, D.W. Ball, S.T. Iacono, S.C. Kettwich, Metastable Nanostructured Metallized Fluoropolymer Composites for Energetics, Journal of Materials Chemistry A 2013, 1(24), 7050-7058.

[43] D.T. Osborne, M.L. Pantoya, Effect of Al Particle Size on the Thermal Degradation of Al/Teflon Mixtures, Combustion Science and Technology 2007, 179(8), 1467-1480.

[44] K.W. Watson, M.L. Pantoya, V.I. Levitas, Fast Reactions with Nano-and Micrometer Aluminum: A Study on Oxidation versus Fluorination, Combustion and Flame 2008, 155(4), 619-634.

[45] S.Y. Fu, X.Q. Feng, B. Lauke, Y.W. Mai, Effects of Particle Size, Particle/Matrix Interface Adhesion and Particle Loading on Mechanical Properties of ParticulatePolymer Composites, Composites Part B: Engineering 2008, 39(6), 933-961.

[46] J. Cho, M.S. Joshi, C.T. Sun, Effect of Inclusion Size on Mechanical Properties of Polymeric Composites with Micro and Nano Particles, Composites Science and Technology 2006, 66(13), 1941-1952.

[47] Cheetah 7.0 [Computer Software]. 2018. Retrieved from Lawrence Livermore National Laboratory, Livermore, California, United States.

[48] ASTM Standard D638, 2014. "Standard Test Method for Tensile Properties of Plastics". ASTM International, West Conshohocken, PA.

[49] Simplify 3D [Computer software]. 2017. Retrieved from https://www.simplify3d.com/

[50] ASTM Standard 7264, 2015. "Standard Test Method for Flexural Properties of Polymer Matrix Composite Materials". ASTM International, West Conshohocken, PA.

[51] O.A. Mohamed, S.H. Masood, J.L. Bhowmik, Optimization of Fused Deposition Modeling Process Parameters: A Review of Current Research and Future Prospects, Advanced Manufacturing 2015, 3(1), 42-53.

[52] M.S. Hossain, J. Ramos, D. Espalin, Improving Tensile Mechanical Properties of FDM-Manufactured Specimens via Modifying Build Parameters, International Solid Freeform Fabrication Symposium: An Additive Manufacturing Conference 2013, Austin, TX, 380-392.

[53] M.S. Uddin, M.F.R. Sidek, M.A. Faizal, Evaluating Mechanical Properties and Failure Mechanisms of Fused Deposition Modeling Acrylonitrile Butadiene Styrene Parts, Journal of Manufacturing Science E-T ASME 2017, 139(8), 081018.

[54] D. Croccolo, M. De Agostinis, G. Olmi, Experimental Characterization and Analytical Modelling of the Mechanical Behaviour of Fused Deposition Processed Parts made of ABS-M30. Computational Material Science 2013, 79, 506-518.

[55] D. Rittel, S. Lee, G. Ravichandran, A Shear-Compression Specimen for Large Strain Testing. Experimental Mechanics 2012, 42(1), 58-64.

[56] ASTM Standard D695, 2015. "Standard Test Method for Compressive Properties of Rigid Plastics". ASTM International, West Conshohocken, PA.

[57] A.M. Peterson, Review of Acrylonitrile Butadiene Styrene in Fused Filament Fabrication: A Plastics Engineering-Focused Perspective, Additive Manufacturing 2019, 27, 363-371.

[58] P. Wolszczak, K. Lygas, M. Paszko, R. A. Wach, Heat Distribution in Material during Fused Deposition Modelling, Rapid Prototyping Journal 2018, 24(3), 615-622.

[59] T.J. Coogan, D.O. Kazmer, Healing Simulation for Bond Strength Prediction of FDM, Rapid Prototyping Journal 2017, 23(3), 551-561.

[60] P.K. Gurrala, S.P. Regalla, Part Strength Evolution with Bonding between Filaments in Fused Deposition Modelling: This Paper Studies How Coalescence of Filaments Contributes to the Strength of Final FDM Part, Virtual and Physical Prototyping 2014, 9(3), 141-149.

[61] J.E. Seppala, S.H. Han, K.E. Hillgartner, C.S. Davis, K. B. Migler, Weld Formation during Material Extrusion Additive Manufacturing, Soft Matter 2017, 13(38), 6761-6769.

[62] A. D'Amico, A.M. Peterson, An Adaptable FEA Simulation of Material Extrusion Additive Manufacturing Heat Transfer in 3D, Additive Manufacturing, 21, 422-430.

[63] C. McIlroy, P. Olmsted, Disentanglement Effects on Welding Behaviour of Polymer Melts during the Fused-Filament-Fabrication Method for Additive Manufacturing, Polymer, 123(8), 376-391.

[64] C. Bellehumeur, L. Li, Q. Sun, P. Gu, Modeling of Bond Formation between Polymer Filaments in the Fused Deposition Modeling Process, Journal of Manufacturing Processes, 6(2), 170-178.

[65] S.A. Tronvoll, T. Welo, C.W. Elverum, The Effects of Voids on Structural Properties of Fused Deposition Modelled Parts: A Probabilistic Approach, The International Journal of Advanced Manufacturing Technology 2018, 97(9-12), 3607-3618.

[66] N.G. Morales, T.J. Fleck, J.F. Rhoads, The Effect of Interlayer Cooling on the Mechanical Properties of Components Printed via Fused Deposition, Additive Manufacturing 2018, 24, 243-248.

[67] M. Spoerk, J. Gonzalez-Gutierrez, J. Sapkota, S. Schuschnigg, C. Holzer, Effect of the Printing Bed Temperature on the Adhesion of Parts Produced by Fused Filament Fabrication, Plastics, Rubber and Composites 2018, 47(1), 17-24.

[68] A.E. Costa, A.F. da Silva, O.S. Carneiro, A Study on Extruded Filament Bonding in used Filament Fabrication, Rapid Prototyping Journal 2019, 25(3), 555-565.

[69] F. Yang, R. Pitchumani, Healing of Thermoplastic Polymers at an Interface under Nonisothermal Conditions, Macromolecules 2002, 35(4), 3213-3224.

[70] R. Pitchumani, S. Ranganathan, R. Don, J. Gillespie, M. Lamontia, Analysis of Transport Phenomena Governing Interfacial Bonding and Void Dynamics during Thermoplastic Tow-Placement, International Journal of Heat and Mass Transfer 1996, 39(6), 1883-1897.

[71] J. Fonseca, I. A. Ferreira, M. de Moura, M. Machado, J. L. Alves, Study of the Interlaminar Fracture under Mode I Loading on FFF Printed Parts, Composite Structures 2019, 214, 316-324.

[72] K. Abinesh, C. Scott, H. Raymond, D. Anagh, K. Ravi, Interlayer Thermal History Modification for Interface Strength in Fused Filament Fabricated Parts, Progress in Additive Manufacturing 2019, 4(3), 63-70.

[73] C.B. Sweeney, B.A. Lackey, M.J. Pospisil, T.C. Achee, V.K. Hicks, A.G. Moran, B.R. Teipel, M.A. Saed, M.J. Green, Welding of 3D-Printed Carbon NanotubePolymer Composites by Locally Induced Microwave Heating, Science Advances 2017, 3(6), 1700262.

[74] A. Tofangchi, P. Han, J. Izquierdo, A. Iyengar, K. Hsu, Effect of Ultrasonic Vibration on Interlayer Adhesion in Fused Filament Fabrication 3D Printed ABS, Polymers 2019, 11(2), 315.

[75] E.M. Liston, L. Martinu, M.R. Wertheimer, Plasma Surface Modification of Polymers for Improved Adhesion: A Critical Review, Journal of Adhesion Science and Technology 1993, 7(10), 1091-1127.

[76] K.M. Praveen, C.V. Pious, S. Thomas, Y. Grohens, Relevance of Plasma Processing on Polymeric Materials and Interfaces, 2019, 1-21.

[77] H. Kim, I.K. Oh, Review of Plasma-Enhanced Atomic Layer Deposition: Technical Enabler of Nanoscale Device Fabrication, Japanese Journal of Applied Physics 2014, 53(3S2), 1-8.

[78] H. Abourayana, P. Dobbyn, D. Dowling, Enhancing the Mechanical Performance of Additive Manufactured Polymer Components using Atmospheric Plasma Pre-Treatments, Plasma Processes and Polymers 2018, 15(3), 1700141.

[79] D.P. Dowling, H.M. Abourayana, T. Brantseva, A. Antonov, P.J. Dobbyn, Enhancing the Mechanical Performance of 3D-Printed Basalt Fiber-Reinforced Composites using In-Line Atmospheric Plasma Pretreatments, Plasma Processes and Polymers 2019, 17(1), 1900143.

[80] C.-C. Shih, M. Burnette, D. Staack, J. Wang, B. L. Tai, Effects of Cold Plasma Treatment on Interlayer Bonding Strength in FFF Process, Additive Manufacturing 2019, 25, 104-111.

[81] R.P. Wool, K.M. OConnor, Time Dependence of Crack Healing, Journal of Polymer Science: Polymer Letters Edition 1982, 20(1), 7-16.

[82] T. Dufour, J. Minnebo, S.A. Rich, E.C. Neyts, A. Bogaerts, F. Reniers, Understanding Polyethylene Surface Functionalization by an Atmospheric He/O_2 Plasma through Combined Experiments and Simulations, Journal of Physics D: Applied Physics 2014, 47(22), 224007.